Formaldehyde and Glyoxal Measurement Deploying a Selected Ion Flow Tube Mass Spectrometer (SIFT-MS)

Antonia G. Zogka, Manolis N. Romanias,[*] and Frederic Thevenet

[1] IMT Nord Europe, Institut Mines-Télécom, Univ. Lille, CERI EE, F-59000 Lille, France

Correspondence to: Manolis N. Romanias (emmanouil.romanias@imt-nord-europe.fr)

Abstract. Formaldehyde (FM) and glyoxal (GL) are important atmospheric species of indoor and outdoor environments. They are either directly emitted in the atmosphere or they are formed through the oxidation of organic compounds by indoor and/or outdoor atmospheric oxidants. Despite their importance, the real-time monitoring of these compounds with soft ionization mass spectrometric techniques, e.g. proton transfer mass spectrometry (PTR-MS), remains problematic and is accompanied by low sensitivity. In this study, we evaluate the performance of a multi-ion selected ion flow tube mass spectrometer (SIFT-MS) to monitor in real-time atmospherically relevant concentrations of FM and GL under controlled experimental conditions. The SIFT-MS used is operated under standard conditions (SC), as proposed by the supplier, and custom conditions (CC), to achieve higher sensitivity. In the case of FM, SIFT-MS sensitivity is marginally impacted by RH, and the detection limits achieved are below 200 ppt. Contrariwise, in the case of GL, a sharp decrease of instrument sensitivity is observed with increasing RH when the H_3O^+ ion is used. Nevertheless, the detection of GL using NO^+ precursor ion is moderately impacted by moisture with an actual positive sensitivity response. Therefore, we recommend the use of NO^+ precursor for reliable detection and quantitation of GL. This work evidences that SIFT-MS can be considered as an efficient tool to monitor the concentration of FM and GL in laboratory experiments and potentially in indoor or outdoor environments, capable of identifying their primary emission or secondary formation through (photo)oxidation processes. Furthermore, SIFT-MS technology still allows great possibilities for sensitivity improvement and high potential for monitoring low proton transfer affinity compounds.

Keywords: SIFT-MS; PTR-MS; Formaldehyde; Glyoxal; H_3O^+; NO^+; charge transfer reaction; quantification.

1. Introduction

Formaldehyde (CH_2O, FM) is the lightest aldehyde. It is a ubiquitous chemical compound in outdoor and indoor environments. FM is a toxic and carcinogenic air contaminant with adverse health effects to humans (Bernstein et al., 1984; Kim et al., 2011). In the open atmosphere, FM is mainly formed by the oxidation of volatile organic compounds (VOCs), (Kefauver et al., 2014). Fuel combustion, forest fires and agricultural activities are also important sources of FM outdoors (Kaiser et al., 2015; Lee et al., 1997; Luecken et al., 2012). FM plays an important role in atmospheric photochemistry since it is photolysed, producing hydroxyl (OH) and hydroperoxy (HO_2) radicals which drive ozone (O_3) production, (Atkinson, 2000). Thus, it enhances the formation of secondary organic aerosol (SOA) (Li et al., 2011). In indoor environments, FM can be emitted directly from wood-based materials, construction materials, paintings, anthropogenic activities such as smoking, cooking, cleaning, or by the oxidation of indoor VOCs, especially terpenes, with high yields (Salthammer, 2019). Indoor concentrations of FM can reach significantly higher levels than outdoors (Crump et al., 1997; Langer et al., 2015; Liu et al., 2006).

Glyoxal ($C_2H_2O_2$, GL) is the lightest α-dicarbonyl compound. GL has been identified as precursor of secondary organic aerosol (SOA) outdoors (Fu et al., 2008; Liggio et al., 2005; Volkamer et al., 2007; Rossignol et al., 2014). GL is formed in the atmosphere by the oxidation of biogenic and anthropogenic VOCs, such as isoprene (the highest emitted VOC in the atmosphere), and acetylene (Fu et al., 2008; Xiao et al., 2007; Myriokefalitakis et al., 2008). The oxidation of aromatic compounds in the presence of NO_x (NO, NO_2) also produces GL. Other sources of GL are biomass burning, fossil and biofuel combustion, (Grosjean et al., 2001; Hays et al., 2002; Kean et al., 2001) as well as oceans, but literature studies report a high variability (Mahajan et al., 2014; Sinreich et al., 2010). In literature it has also been reported that the photochemical oxidation of GL in the troposphere leads to HO_x radical formations (Salter et al., 2013). In indoor environments, to the best of our knowledge, there are no studies reporting the direct emission or secondary formation of GL, but, considering emerging research activities dealing with indoor air quality, this should not be excluded.

Due to their important role in the chemistry of outdoor and indoor environments, the monitoring of the FM and GL in laboratory experiments (e.g. simulation chamber experiments, photochemical reactors) or in field (indoor and outdoor) is of significant importance in order to evaluate and understand the underlying chemistry. Nevertheless, the real time measurement of FM and GL is not a trivial process. The sensitivity of the classically used proton transfer mass spectrometry (PTR-MS) technique for these compounds is quite limited and is strongly impacted by relative humidity (Inomata et al., 2008; Stönner et al., 2017; Vlasenko et al., 2010; Yuan et al., 2017). Limitations are mainly due to the low proton transfer affinities (PA) of both compounds of interest : $PA_{FM} = 713$ kJ mol^{-1} and $PA_{GL} = 675\text{-}690$ kJ mol^{-1} (Wróblewski et al., 2007), and thus very close to the PA of water, $PA_{H2O} = 691$ kJ mol^{-1}. Quite recently, electron attachment reaction (EAR) ionization mass spectrometry has been used for real-time measurements of GL in ambient air. Nevertheless, this technique does not seem to be sensitive enough for other volatile organic compounds (VOCs) (Lu et al., 2019). It should be noted that mass spectrometric techniques are widely applied in atmospheric science for three main reasons. First, they are sensitive tools, able to monitor simultaneously and in real-time a wide range of VOCs. Second, they are robust, user-friendly and mobile systems. Third, they require a relatively low sampling flow (in the order of hundred cm^3 min^{-1}) and can be easily coupled to "small scale" laboratory experiments or with other instrumentation without a significant extra demand on air sampling flow.

75
76 Alternatively, the monitoring of FM and GL is achieved using VOC-selective spectroscopic techniques
77 such as Fourier transform infrared spectroscopy (FTIR) (Catoire et al., 2012), differential optical absorption
78 spectroscopy (DOAS) (Coburn et al., 2014), tunable-diode laser absorption spectrometer (TDLAS) (Catoire
79 et al., 2012), or incoherent broadband cavity-enhanced absorption spectrometer (IBBCEAS) (Liu et al.,
80 2019; Lu et al., 2019). FTIR spectroscopy is mostly used in lab experiments (Catoire et al., 2012) deployed
81 in-situ or in line configuration inside atmospheric simulation chambers or photoreactors (Wisthaler et al.,
82 2008). However, the sensitivity is relatively poor and even long optical path FTIR systems achieve detection
83 limits (DL) in the order of several parts per billion (ppb). In addition, long path FTIR systems are not
84 mobile, or of limited mobility, and the selective detection of FM and GL is relatively difficult due to the
85 complex IR pattern in the presence of other VOCs. Other VOC-selective spectroscopic tools such as DOAS
86 and IBBCEAS, are mostly used in outdoor field studies (Coburn et al., 2014; Lu et al., 2019). These are
87 expensive and delicate systems that can achieve detection limits in the sub-ppb level. However, these
88 techniques require a high volume sampling flow of several liters per minute (L min^{-1}) (Coburn et al., 2014;
89 Lu et al., 2019). Thus, they are not commonly deployed in laboratory studies or indoor field measurements.
90 Therefore, low time resolution techniques such as off-line analytical approaches are used for the selective
91 determination of FM and GL. In particular gas chromatography and mass spectrometry (GC-MS), or high-
92 performance liquid chromatography (HPLC) are used for off line analysis of sampling cartridges (Ban-
93 Weiss et al., 2008; Gómez Alvarez et al., 2012; Wisthaler et al., 2008).
94
95 A response to the need for real-time, selective and sensitive monitoring of FM and GL could be the selected
96 multi-ion flow tube mass spectrometry (SIFT-MS). SIFT-MS is a soft ionization analytical technique,
97 mainly used for the real time monitoring (identification and quantification) of a wide diversity of VOCs,
98 and some inorganic species (e.g. NO_2, HONO). SIFT-MS attains the advantages of typical mass
99 spectrometric techniques described above. SIFT-MS is essentially a double quadrupole chemical ionization
100 mass spectrometer using simultaneously H_3O^+, NO^+, and O_2^+ precursor ions for the ionization and the
101 subsequent detection of the analytes. SIFT-MS has extensively been used for breath analysis, and in food
102 science, but it is not commonly used in atmospheric science, where traditionally, PTR-MS is widely applied.
103 Nevertheless, in the last decade, the application of SIFT-MS technology for the study of atmospheric
104 relevant processes became more frequent, where SIFT-MS is either coupled to experimental chambers with
105 various volumes for indoor studies(Caron et al., 2016; Caron et al., 2020; Thevenet et al., 2021), or
106 atmospheric simulation chambers for the study of VOC degradation (Osseiran et al., 2020; Allani et al.,
107 2021).
108
109 Quite recently, Lacko et al. (2020) have reported for the first time the detection of FM and GL deploying a
110 custom made SIFT-MS. In their study, authors mainly focus on the ion chemistry occurring inside the flow
111 tube of the instrument and how it is impacted by humidity. These authors have also applied chemical
112 modeling in an attempt to interpret their experimental results. Nevertheless, Lacko et al. (2020) used a
113 custom-made SIFT-MS instrumentation that was operated in a tailored mode, injecting the corresponding
114 VOC in a humidified air flow of helium bath gas. Their measurements were carried out at low levels of
115 relative humidity, never exceeding 10 %, and using constant concentrations of VOCs in the ppm range.
116 Therefore, authors did not evaluate the response of the instrument in a VOC concentration span of sub-ppm
117 range, typical of indoor and outdoor environments, and they did not report the corresponding detection
118 limits (DL). Furthermore, their study was solely focused on the chemistry of H_3O^+ precursor ion.

119

120 In this paper, we present a series of calibration experiments of FM and GL deploying a commercially
121 available SIFT-MS Voice 200 Ultra instrument. The main objective of this work is to evaluate the
122 sensitivity of SIFT-MS towards FM and GL, and elucidate whether it can (i) be used to monitor the
123 concentrations of the title compound in laboratory scale or ambient indoor / outdoor air conditions and (ii)
124 overcome the limitations encountered in conventional PTR-MS studies as highlighted above. In addition,
125 for the first time in literature, we aim to emphasize the importance of NO^+ charge transfer reactions on the
126 detection of GL. To meet these objectives, FM and GL calibration measurements are carried out under
127 dynamic flow conditions using a wide range of VOC concentrations in the ppb level, varying the relative
128 humidity (RH) from dry to 70 %. Within that framework we assess the impact of RH and the instrument
129 operational conditions (i.e. pressure and temperature) to its performance.

130

131 The structure of the article is as follows: first we present a detailed description of the experimental set up,
132 the methods deployed and protocols followed in this work. Thereafter, in the results and discussion section
133 we provide (i) literature and experimental evidences that impact charge transfer reactions in SIFT-MS and
134 PTR-MS, and (ii) the actions made in the framework of our study to improve SIFT-MS performance.
135 Subsequently, results and discussion on FM and GL are presented separately in two different sections. Each
136 of the two subsections include the presentation of our experimental observation, and a thorough discussion
137 that contains comparison with PTR-MS or other SIFT-MS studies, and comprehensive assessment of the
138 charge transfer reactions involved in the detection of the compound of interest.

139

140 ## 2. Experimental Section

141 ### 2.1 Materials

142 **Formaldehyde source.** A gas cylinder of FM purchased from praxair (12 ppm in N_2) is used as a source
143 for the calibration experiments. The purity and stability of the gas mixture is regularly tested by sampling
144 FM gas on DNPH cartridges (Waters) eluted and analyzed off-line using UltiMate 3000 HPLC instrument
145 (Thermo Scientific) coupled with an ultraviolet detector.

146 **Glyoxal source.** The monomer of pure GL is synthesized applying a similar method with the literature
147 (Volkamer et al., 2005). In particular, equal amounts (ca. 0.6 g) of GL trimer dihydrate (purity $\geq$ 97 %
148 Sigma-Aldrich) and di-phosphorous pentoxide (purity > 98 %, VWR Chemicals) are mixed in a glass bulb
149 and are progressively heated up under vacuum (1.5×10^{-3} Torr) from room temperature to 453 K. The
150 evolving gas is collected in a glass trap immersed into liquid nitrogen where the bright yellow pure GL
151 solid crystals appear. Subsequently, after synthesis, the cold trap containing the monomer of GL is placed
152 in a liquid nitrogen/ethanol bath maintained at 230 K, and is degassed under vacuum several times to
153 remove volatile by-products (purification process). The vapors of pure GL are collected in a 10 L Pyrex
154 glass bulb, darkened to minimize exposure of the sample to room light. The purity of the gas is verified by
155 FTIR spectroscopy deploying an Antaris FTIR spectrophotometer equipped with a 2 L optical gas cell with
156 10 m optical path length. The temperature of the optical cell is maintained at 353 K. The FTIR spectra
157 collected are of high quality and identical to those presented in literature for pure GL monomers (Volkamer
158 et al., 2005). The thermal stability of the GL is also verified, and we evidence that no thermal decomposition
159 occurs, in accordance with the literature (Feierabend et al., 2008; Saito et al., 1984). Considering the
160 detection limits of the instrument for CO, CO_2 (in the order of 0.1 ppm), and FM (in the order of 1 ppm,
161 the purity of GL is greater than 99 %. After the quality control experiments, dilutions of GL gas in He are

162 prepared manometrically in another glass bulb, with mixing ratios of ca. 1 % for a total pressure of 400
163 Torr. For the sake of simplicity it will be referred to as mixture 1 (GL diluted in He) in the following.
164 Mixture 1 is used as a source to prepare more diluted GL/He gas mixtures (in the range of 50 to 120 ppm)
165 with total pressure of 1550 Torr inside a 6 L silonite treated canister. The exact concentration of GL in the
166 canister is determined with FTIR spectroscopy using the well-defined broad band IR absorption cross
167 section coefficients provided in literature for the characteristic band of GL between 2724-2940 cm^{-1}
168 (Volkamer et al., 2005). These mixtures are used for the calibration of the SIFT-MS instrument and their
169 stability is evaluated on a daily basis. It should be noted that two different GL syntheses were carried out
170 and 4 different GL+He canister mixtures are used for the calibration experiments to evaluate uncertainties
171 related to GL concentration.
172

2.2 Experimental Setup

General Description

176 The experimental set up used in the current study is reported in Fig. 1. The gas flow generation lines are
177 made of Teflon. Calibrated mass flow controllers (MFC) are used to mix the flow of the target VOC (i.e.
178 FM or GL) with dry or humid zero air (impurity levels: VOCs < 0.1 ppb, CO_2 < 10 ppb, and CO < 80 ppb,
179 moisture level: ca. 2 ppm). The total gas flow rates in the calibration measurements are in the order of 1000
180 mL min^{-1}. Nevertheless, experiments are also performed varying the flow rate between 300 to 1600 mL
181 min^{-1} aiming to evaluate the possible loss of compounds on gas lines. The total concentration of the target
182 VOCs in the diluted gas flow are between 40 to 1200 ppb. In the case of FM, the diluted gas stream is
183 sampled by an ap2e ProCeas FM analyzer (sampling rate 180 mL min^{-1}) and the SIFT-MS (sampling rate
184 35 mL min^{-1}) connected in parallel. Concerning GL calibration experiments, the FM analyzer and the long
185 path FTIR were occasionally used to evaluate possible impurities in the canister or transformation of GL in
186 the gas lines, but the majority of the measurements are carried out by-passing them.

187
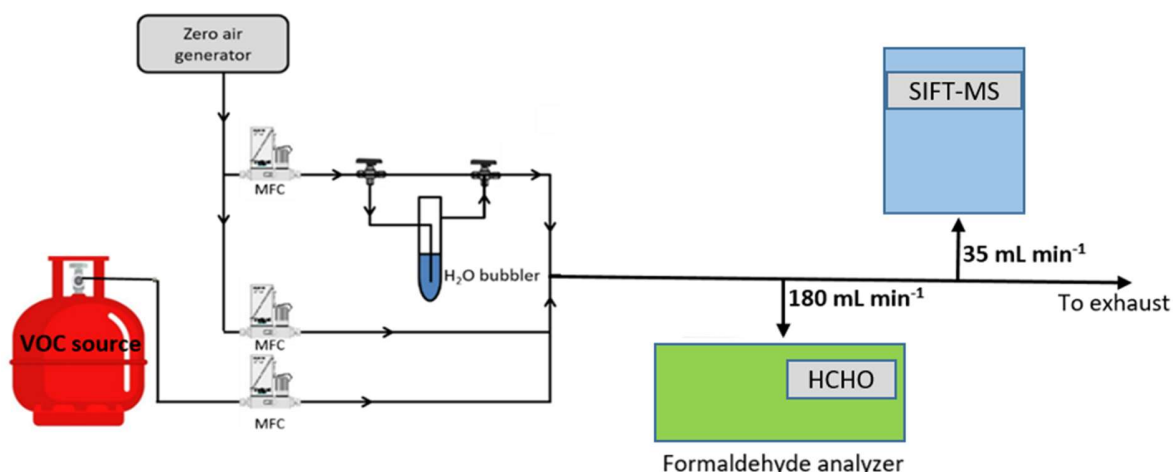
Figure 1. Experimental set-up used in the framework of the current study.

Formaldehyde analyzer ap2e ProCeas
The real time measurement of FM in the gas flow is achieved deploying an ap2e ProCeas gas analyzer. The gas flow is sampled through a sonic orifice with a diameter of few micrometers. Then, the gas is driven to an optical cell and analyzed employing patented laser optical feedback cavity enhanced absorption infrared spectroscopy. The instrument response is ca. 2 seconds and the detection limit (3σ) of FM is 1 ppb for an integration time of 1 minute.

SIFT-MS
The SIFT-MS voice 200 ultra (Syft technology) is a double quadrupole chemical ionization mass spectrometer. A microwave discharge generates simultaneously three precursor ions, H_3O^+, NO^+ and O_2^+, which are sequentially selected by a first quadrupole mass filter (Smith and Španěl, 2005). Then, under a flow of He, used as carrier gas, the precursor ions are driven inside a low pressure flow tube reactor. At the same time, the sampling flow is injected at the upstream-end of the reactor. The precursor ions react with the analytes along the flow tube to form characteristic ionized molecules as reaction products (Smith and Španěl, 2005). The temperature of the sampling port and the flow tube are temperature regulated (293 – 393 K) to avoid contaminations of the sampling line and adsorption of reactants along the flow tube. Subsequently, the gas stream passes through a skimmer, located at the downstream end of the flow tube reactor, and finally is injected in a high vacuum chamber where both the precursor and reaction product-ions are focused, via electrostatic lenses, into a second quadrupole for mass analysis and ion counting. At this point it should be noted that the simultaneous presence of the three precursor ions allows the real-time monitoring of several VOCs eliminating the effect of mass peak overlapping due to the use of a quadrupole mass filter with a low mass resolution. Interestingly, this multi-ion chemistry allows SIFT-MS to discriminate isobaric compounds (Guimbaud et al., 2007), which is not a trivial task even for time of flight (TOF) techniques (Stönner et al., 2017; Yuan et al., 2017).

FTIR
The purity of the glyoxal is verified by FTIR spectroscopy deploying an Antaris FTIR spectrophotometer equipped with a 2 L optical gas cell with 10 m optical path length and zinc selenide transmission windows. The temperature of the optical White-cell is maintained at 353 K. A liquid-N_2 cooled mercury cadmium telluride (MCT) detector was attached and 64 co-added IR spectra were recorded between 650 and 4000 cm^{-1}, with 1 cm^{-1} resolution, using Result-3 software. Quantification and data processing were performed using a thermos scientific software, TQ-AnalystTM.

2.3 Experimental Procedure and Detection Limits

Figure 2 displays the experimental strategy followed in the framework of the current study to calibrate the SIFT-MS. In a typical calibration experiment, initially the background of the VOC of interest is monitored for at least 20 min under a stream of zero air at the selected RH. Then the desired level of VOC is introduced in the gas stream and its concentration is monitored in real time. In each calibration step the flows are kept constant for around 20 min. In case of FM, the stabilization of its concentration in the gas flow is achieved

231 within the first 10 min after its introduction in the gas flow while in case of GL, its concentration is
232 stabilized almost instantaneously. Typically 4 to 6 different concentration levels of the VOC of interest are
233 set in each calibration experiment. At the end, the background is recorded again. This experimental
234 procedure is repeated for each level of RH and for each VOC individually. In the case of FM the calibration
235 factor is determined by plotting the SIFT-MS response (in counts) versus the concentration reported by the
236 FM analyzer; while in the case of GL by plotting the SIFT-MS response as a function of GL concentration
237 determined by the measured flow rate and the sample mixing ratio.

239 The time resolution of the SIFT-MS instrument in the calibration experiments is set to 1 second. FM is
240 monitored at the mass peak m/z $=31$ (CH_3O^+, FM-H$^+$) arising from H_3O^+ precursor ion, while in the case
241 of GL the mass peaks m/z $=59$ ($C_2H_3O_2^+$) and m/z$=88$ ($C_2H_2O_2 \cdot NO^+$), originating from H_3O^+ and NO^+
242 respectively are used.
243 To determine the detection limits (DL) of the SIFT-MS Eq. (1) is used:
244 $$DL = \frac{3.3 \times SD}{calibration\ factor} \qquad \text{Eq. (1)}$$
245 where SD is the standard deviation of the background signal. Similar criterion has been used in literature to
246 determine the detection limits of PTR-MS instruments for FM and GL. Therefore, it will allow to make a
247 direct comparison between the instrument sensitivities.
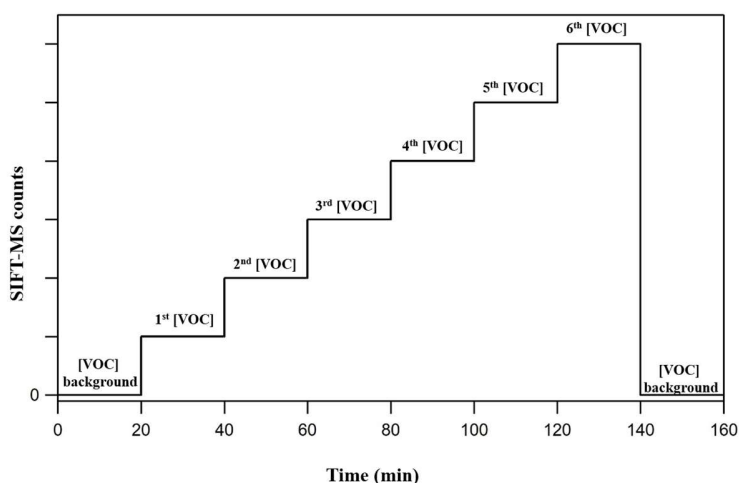
249

Figure 2. Strategy followed during a typical calibration experiment. At first, the background of the VOC at
the corresponding mass peak(s) is recorded. Then its concentration is progressively increased and monitored
with SIFT-MS. Typically, 4 to 6 different concentrations of the VOC of interest are set before returning to
background monitoring.

3. Results and Discussion

251 Results and discussion section is divided in three parts. In the first one, we discuss the optimization of
252 operational parameters and conditions of the SIFT-MS and the strategy followed to improve the method
253 and the performance of the instrument. The second and the third subsections are dedicated to the calibration

measurements of FM and GL respectively, as a function of RH under standard and custom SIFT-MS operational conditions.

3.1 From Standard to Custom Method for SIFT-MS Determination of FM and GL

The standard operational conditions (SC) of the SIFT-MS, as recommended by the supplier, correspond to: (i) temperature of 393 K for the sampling plate and the flow tube, (ii) He flow rate of 380 mL min^{-1} as bath gas, (iii) sampling flow rate of 35 mL min^{-1}, resulting in a total pressure inside the flow tube of 0.65 Torr (Table 1). Table 1 summarizes other characteristic parameters of the SIFT-MS such as carrier gas (v_g) and ions flow (v_i) velocities, reaction time inside the flow tube of the instrument (t_r), mean kinetic energy between reactants (KE_{cm}). However, literature studies have reported that FM and GL detection is highly sensitive to operational conditions of soft ionization mass spectrometers (Lacko et al., 2020; Stönner et al., 2017; Yuan et al., 2017). In particular, the detection of FM and GL is based on association reactions, (Lacko et al., 2020; Michel et al., 2005; Stönner et al., 2017; Yuan et al., 2017) and thus the pressure and temperature of the flow tube can play a dominant role since association reactions are favored at higher pressures. Furthermore, in literature the fragmentation of GL has been reported, leading to reduced sensitivity and a more complex chemistry inside the reaction tube of the corresponding mass spectrometer (Lacko et al., 2020; Stönner et al., 2017). Crucial role for the detection of both FM and GL is also played by the KE_{cm} (Hansel et al., 1997).

Considering the abovementioned challenges related to the sensitive detection of FM and GL, to improve the sensitivity of the SIFT-MS we modified the pressure and temperature conditions of the SIFT-MS compared with SC. In particular, we indirectly increased the pressure inside the flow tube, by increasing He flow to its maximum value of 500 mL min^{-1}, under constant pumping. This increase in He flow results in a 23 % higher pressure compared with SC. The temperature of the flow tube and sampling plate has been decreased to 323K. The temperature decrease results in lower KE_{cm}. Combined with increasing pressure, it leads to lower gas and ion flow velocities, and longer reaction times in the flow tube. Based on the literature (as described below, experimentally validated in our study), these modifications are anticipated to increase the sensitivity of the instrument. These modified operation conditions of the SIFT-MS are summarized in Table 1. In the following of the manuscript, they are referred to as custom conditions (CC). In order to assess the relevance of CC, calibration experiments described in the following of the manuscript are carried out under both SC and CC conditions.

Table 1. SIFT-MS parameters and conditions used in the framework of the current study.

Parameters	Standard operation conditions (SC)	Custom operation conditions (CC)
Flow tube length,[a] L (cm)	34	
Flow tube internal diameter, D (cm)	4.1	
Sample plate temperature (K)	393	323

Flow tube temperature, T_g (K)	393	323
Flow tube pressure (Torr)	0.65	0.85
Molecular density in the flow tube, N (molecule cm^{-3})	1.6×10^{16}	2.5×10^{16}
Carrier gas flow (mL min^{-1})	380	500
Carrier gas flow rate, F_g (Torr L s^{-1})	5.12	6.69
Carrier gas flow velocity,[b] v_g (cm s^{-1})	860	705
Ion flow velocity,[c] v_i (cm s^{-1})	1290	1058
Reaction time,[d] t_r (ms)	27.5	33.5
Mean kinetic energy between reactants,[e] KE_{cm} (eV)	0.05	0.04
H$_2$O concentration range injected in the flow tube,[f] (molecule cm^{-3})	$(0.01\text{-}943)\times10^{12}$	$(0.02\text{-}1160)\times10^{12}$
FM concentration range injected in the flow tube,[g] (molecule cm^{-3})	$(0.68\text{-}13.6)\times10^{8}$	$(0.83\text{-}16.6)\times10^{8}$
GL concentration range injected in the flow tube,[g] (molecule cm^{-3})	$(0.68\text{-}16.9)\times10^{8}$	$(0.83\text{-}20.0)\times10^{8}$

[a]: Distance between sample flow injection point and the end of the flow tube; [b]: calculated from the expression $v_g = \frac{4F_g T_g}{P_g \pi D^2 273}$ where F_g is the carrier gas flow rate, T_g the temperature of the carrier gas, P_g the pressure in flow tube, and D the flow tube internal diameter;(Španěl and Smith, 1996) [c]: calculated as $v_i = 1.5 \times v_g$;(Smith and Adams, 1988) [d]: estimated from the expression $t_r = \frac{L+\varepsilon}{v_i}$ where $\varepsilon = 1.5$ and corresponds to the distance for a full mixing of neutral molecules with the carrier gas in the flow tube; [e]:calculated using the recommended expressions by Hansel et al. (1997). $KE_{cm} = \frac{m+M}{M}(KE_{ion} - 1.5k_B T) + 1.5k_B T$ where m and M are the masses of the carrier gas and the neutral reactant, respectively, k_B is the Boltzmann constant and KE_{ion} is the kinetic energy of ions obtained by the expression $KE_{ion} = 1.5k_B T + 0.5mv_i^2 + 0.5M_{ion}v_i^2$, where M_{ion} is the mass of reactant ion; [f]: estimated using the following expression $[H_2O] = \frac{F_{H_2O}}{F_{total}} \times N$, where F_{H_2O} is the sample flow of pure water in the sample flow calculated as the product of RH with the total sample flow rate (35 mL min^{-1}), F_{total} the total flow rate inside the flow tube, and N the number density; [g]: calculated in a similar way with water concentrations, $[VOC] = \frac{F_{VOC}}{F_{total}} \times N$ where F_{VOC} is the sample flow of pure VOC in the sample flow calculated as the product of VOC mixing ratio in the total sample flow (35 mL min^{-1}).

We observed that operating the instrument under SC or CC modes has a negligible impact on the concentration of the NO$^+$ and O$_2^+$ primary ions. However, the distribution of H$_3$O$^+$ and H$_3$O$^+\cdot$H$_2$O clusters is influenced. The hydronium water cluster can be formed from (R1):

H$_3$O$^+$ + H$_2$O + M → H$_3$O$^+\cdot$H$_2$O + M   (R1)
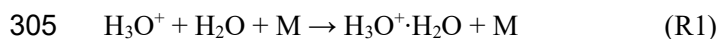
306 The rate coefficient of (R1) is $k_1(298 \pm 2K) = (6.55 \pm 0.75) \times 10^{-28}$ cm^6 s^{-1}. It is an average value
307 retrieved from three literature studies (Bierbaum et al., 1976; Bolden and Twiddy, 1972; Španěl and Smith,
308 2001). The errors quoted correspond to the standard deviation of the measurements.

310 Reaction 1 is an association reaction, and therefore the rate coefficient depends on the thermal stabilization
311 of the adduct leading to the formation of $H_3O^+ \cdot H_2O$, favored at low temperatures and high pressures.
312 Consequently, both temperature and pressure modifications, applied to establish CC, enhance the formation
313 of $H_3O^+ \cdot H_2O$ clusters. In addition, reaction time also plays a role. Under CC, t_r is increased by a factor of
314 1.22 compared to SC, and thus an increase in the concentration of $H_3O^+ \cdot H_2O$ is expected. In order to
315 establish a criterion for the humidity adjustments during the calibration experiments and the different
316 operation modes of the instrument , the ratio of the signals for the $H_3O^+ \cdot H_2O$ cluster at the m/z 37 (I_{37}) and
317 H_3O^+ at the m/z 19 (I_{19}) is considered. Note that similar approaches have been applied in literature.(Inomata
318 et al., 2008; Stönner et al., 2017) In Fig. S1 are presented these relative ratios of I_{37}/I_{19} versus the RH in the
319 gas flow for the two different operation modes of the SIFT-MS. It should be noted that, as displayed in Fig.
320 S1 when ambient water vapor concentration is close to zero level, i.e. close to dry conditions, the I_{37}/I_{19}
321 ratio approaches zero pointing that the water coming from the discharge ion source entering the flow tube
322 is negligible compared to water vapor from the sampled dry air. This is in contrast with what has been noted
323 in PTR-MS studies (Inomata et al., 2008; Stönner et al., 2017).

325 In theory, it is possible to estimate the water concentration inside the flow tube to better predict the changes
326 on the abundances of H_3O^+ and $H_3O^+ \cdot H_2O$ ions. Lacko et al. (2020), applied the following expression to
327 estimate the water concentration:

328 $$[H_2O] = \frac{H}{t_r k_1} \qquad \text{Eq. (2)}$$

330 where $H = ln\frac{[H_3O^+] + [H_2O \cdot H_3O^+] + [(H_2O)_2 \cdot H_3O^+]..}{[H_3O^+]}$ Eq. (3)

331 However, in the literature, k_1 has solely been determined at room temperature, thus extrapolation cannot be
332 directly performed to SC or CC. Alternatively we can use the mixing ratios of water in the sample flow to
333 estimate the concentration of water molecules introduced in the flow tube (Table 1). The background [H_2O]
334 has been estimated in the range of 10^{10} molecule cm^{-3} (based on H_2O residual levels in the zero-air flow,
335 <2ppm corresponding to RH <0.01%), while the increase in RH resulted in water concentrations introduced
336 in the flow tube in the order of 10^{14} molecule cm^{-3}, corresponding to around 5 % of the total number density.
337 A similar approach was applied to estimate the concentrations of FM and GL inside the flow tube. Using
338 mixing ratios of 50 up to 1200 ppb in the sample flow, the concentrations of the title VOCs were in the
339 range of 10^8 molecule cm^{-3}, and thus several order of magnitude lower than [H_2O].

340 ## 3.2 Formaldehyde Determination using SIFT-MS

342 **3.2.1 Experimental Calibration of Formaldehyde under SC and CC**

343 Figure 3 displays typical calibration curves of FM operating SIFT-MS under standard and custom
344 conditions. The slope of the linear fit of experimental results corresponds to the calibration factor of the
345 compound of interest. In both cases, a linear response ($R^2 > 0.997$) of the instrument is noticed on the entire
346 concentration range explored. However, at 70% of RH the experimental data points are more scattered
347 resulting in a lower precision fit. In Table 2 are summarized the calibration factors at each I_{37}/I_{19} ratio.
348 Under CC, the sensitivity of SIFT-MS towards FM is increased by a factor of ca. 2, compared to SC. In
349 addition, considering the experimental uncertainties, under SC, the SIFT-MS response is not influenced by
350 the level of RH used while under CC the sensitivity of the instrument is reduced by a factor of 2 from dry
351 ($I_{37}/I_{19} < 0.01$) to 70% ($I_{37}/I_{19} = 1$). Actually, a careful look at the data presented in Table 2 points that SIFT-
352 MS sensitivity is not impacted by water presence when the relative ratio of I_{37}/I_{19} is below ca. 0.55,
353 irrespectively of the SIFT-MS operation mode. Under CC, to express the relative humidity dependence of
354 the instrument sensitivity at the mass peak 31, the calibration factors were plotted as a function of the I_{37}/I_{19}
355 ratio, using a weighted fit power function (Fig. S2). The weighted fitting considers the uncertainties denoted
356 for each calibration factor. The following expression describes the instrument sensitivity under SC for the
357 mass peak 31:

358 $$C_F^{31}(counts\ ppb^{-1}) = 162 - 82.3 \left(\frac{I_{37}}{I_{19}}\right)^{2.41} \quad \text{Eq. (4)}$$

359
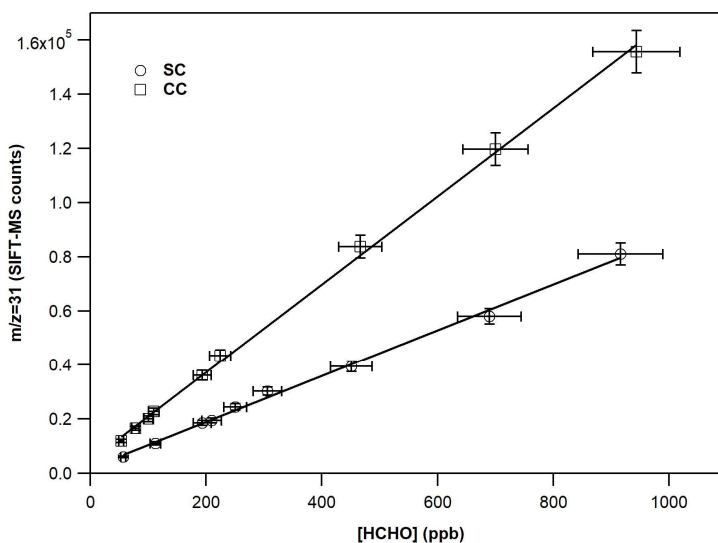
360
361
362 **Figure 3.** Calibration curves of FM at the m/z 31, derived from H_3O^+ precursor ion under dry conditions.
363 The error bars on Y axis are 5 % (extreme value) and correspond to the 2σ standard deviation of the
364 averaged value of the SIFT-MS signal for each measurement. The errors reported in X axis are 8 % and
365 correspond to the uncertainty given for the cross section value of FM (4%) and other systematic
366 uncertainties (in the flow of the mixture, sampling flow of the instrument, etc.) added in quadrature.

367 **Table 2.** Calibration factors and detection limits of FM at the m/z = 31 as a function of relative humidity
368 for standard and custom operational conditions of the SIFT-MS. The calibration factor is derived from the
369 slope of a typical experiments shown in Fig. 3. The errors given in the calibration factors are the 2σ precision
370 of the linear fit.

RH gas flow (%)	Standard Operational Conditions			Custom Operational Conditions		
	I_{37}/I_{19}	Calibration factor (counts ppb^{-1})	Detection limits (ppt)	I_{37}/I_{19}	Calibration factor (counts ppb^{-1})	Detection limits (ppt)
Dry	0.001	84.8±3.8	400	0.005	163±4	100
10	0.09	88.4±6.2		0.28	148±6	120
30	0.26	83.0±2.2		0.56	145±4	
50	0.41	82.7±1.0		0.79	115±5	145
70	0.54	70.0±12	500	1.0	82.5±14	200

Contrariwise, in literature it is reported that the sensitivity of a PTR-MS is massively reduced with RH. For instance, in the study of Stönner et al. (2017), the PTR-MS sensitivity was reduced by a factor of five or even greater when the relative ratio of $H_3O^+ \cdot H_2O$ to H_3O^+ masses (measured as I_{39}/I_{21}) varies from <0.1 to 0.4.

3.2.2 Comparison of Formaldehyde Determination between SIFT-MS and PTR-MS

The contrasted behavior between the SIFT-MS and PTR-MS instruments are related to their distinct operational principles and chemical reactions. Therefore, before getting into the chemistry of proton transfer reactions for FM measurement, it is essential to discuss the major differences between the conditions inside the flow tube of the SIFT-MS used in the current study and inside the drift tube of the PTR-MS instruments deployed in literature for FM characterization (Inomata et al., 2008; Stönner et al., 2017; Vlasenko et al., 2010; Warneke et al., 2011).

The pressure inside the flow tube of the voice 200 Ultra SIFT-MS instrument ranges between 0.6 to 0.9 Torr (Table 1), which is by a factor of two lower than the pressure inside the drift tube in a PTR-MS. This pressure difference can impact the ion chemistry and mainly the formation of $H_3O^+ \cdot H_2O$ clusters. Besides pressure, the main difference between the two instruments relies in the mean relative kinetic energy of reactants (KE_{cm}). In the flow tube of the SIFT-MS the KE_{cm} of analytes and precursor ions depend mainly on the temperature of the tube. Under the SC and CC the kinetic energy was calculated to be ca. 0.05 and 0.04 eV respectively (Table 1). On the contrary the application of an electrical field inside the drift tube of a PTR-MS leads to significantly higher KE_{cm} values, reducing the sensitivity of the instrument. Typical values of KE_{cm} range between 0.10 to 0.23 eV in studies using PTR-MS for FM monitoring (Table 3), (Inomata et al., 2008).

Ion Chemistry Involved in Formaldehyde Measurement with H_3O^+ Precursor Ion

The proton transfer reaction in case of FM can occur according to the following reaction:

$$CH_2O + H_3O^+ \rightarrow CH_3O^+ + H_2O \qquad (R2a)$$
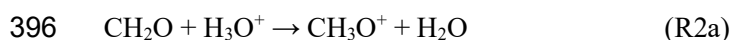
The rate coefficient of (R2a), k_{2a} is in the order of 3×10^{-9} cm^3 s^{-1} at 297±3 K (Michel et al., 2005) (Table 3), and slightly dependent on KE_{cm}.

399   However, due to the low exothermicity of (R2a) the back reaction is also possible:

400    $CH_3O^+ + H_2O \rightarrow CH_2O + H_3O^+$ (R2b)
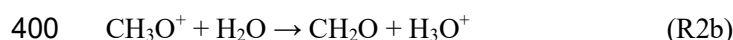
401   Hansel et al. (1997) evidenced that (R2b) is strongly dependent on the KE_{cm} values of reactants. The highest
402   the KE_{cm} of protonated FM (FM-H$^+$), the highest the probability for a successful collision. Thus, the rate
403   coefficient of deprotonization reaction k_{2b} increases. Table 3 summarizes the values of k_{2b} for different KE_{cm}
404   used in PTR-MS studies and under SC or CC conditions of the SIFT-MS. Furthermore, (R2b) also depends
405   on the concentration of water molecules when evaluating the response of the SIFT-MS and PTR-MS
406   instruments as a function of RH. Therefore, the contribution of these two parameters, i.e. KE_{cm} of reactants
407   and water concentration inside the reaction tubes, may explain the contrasted behaviors between the two
408   instruments. In SIFT-MS, due to the low kinetic energy of reactants, the protonation of FM is strongly
409   favored. Indeed, k_{2a}/k_{2b} ratio is ca.1600 and ca.5300 respectively under SC and CC. It has to be noted that
410   an increase of water concentration due to RH variation in the analytes shows a negligible impact on the
411   k_{2a}/k_{2b} ratio. It can also be suggested that the higher k_{2a}/k_{2b} ratio under CC could explain the amplification
412   by a factor of ca. 1.9 of FM sensitivity compared to SC. On the contrary, in the case of PTR-MS where
413   higher kinetic energies are achieved, the relative ratio of k_{2a}/k_{2b} remains below 160 and possibly goes down
414   to 26. Thus, a substantial increase of water concentration makes (R2b) more impactful and the sensitivity
415   of the instrument is strongly decreased.

416   **Table 3.** Rate coefficients of ion-molecule chemical reactions of FM under typical PTR-MS studies
417   retrieved from literature and the conditions where SIFT-MS is deployed in this work.

Values	PTR-MS[a]			SIFT-MS	
				Standard operational conditions	Custom operational conditions
KE_{cm} (eV)	0.10	0.17	0.23	0.05	0.04
k_{2a} (10^{-9} cm^3 s^{-1})	1.6	1.4	1.3	3.2[b]	3.2
k_{2b} (10^{-11} cm^3 s^{-1})	1.0	2.9	5.0	0.2[b]	0.06[c]
k_{3a} (10^{-9} cm^3 s^{-1})	-	-	-	2.65±0.35[d]	-
k_{3b} (10^{-10} cm^3 s^{-1})	-	-	-	4.4±1.1	-
k_4 (10^{-11} cm^3 s^{-1})	Negligible			1.2	>1.2
k_{2a}/k_{2b}	160	48	26	1600	5333
k_4/k_{2b}	Negligible			6	>20

418 [a]: data retrieved from the work of Inomata et al. (2008). Authors extracted the k_{2a} and k_{2b} values based on the work of
419 Hansel et al. (1997); [b]: average value determined by Hansel et al. (1997) ; [c] calculated by Bohme et al. (1979); [d]:
420 average literature value from the studies of Bohme et al. (1979) and Midey et al. (2000). The error corresponds to the
421 standard deviation of the measurements.

422 Although solely the m/z = 31 is used to monitor FM, in SIFT-MS other ion reactions can occur and form a
423 protonated methyl hydroperoxide (PMH) complex with m/z = 49 (Hansel et al., 1997). These ion reactions
424 are not expected to occur in PTR-MS due to the high KE_{cm} values. These reactions are strongly dependent
425 on water concentrations in the flow tube, and they are competitive to (R2a) and (R2b). However, their
426 contribution to the ion chemistry inside the flow tube of the SIFT-MS is expected to be of minor importance,
427 especially under SC. Indeed, under SC the calibration factor of FM is not impacted by increasing water
428 concentration by almost 540 times (considering the I_{37}/I_{19} ratios calculated under dry and 70 % of RH).
429 However, since their occurrence cannot be excluded and they could play a role for I_{37}/I_{19} ratios above 0.55,
430 these reactions are discussed in the following of the manuscript.

431 The protonation of FM can occur through ligand switching from the hydronium water cluster, $H_3O^+·H_2O$
432 and to form PMH through the following reaction:

433 $$H_3O^+·H_2O + CH_2O \rightarrow CH_3O^+·H_2O + H_2O \qquad (R3a)$$
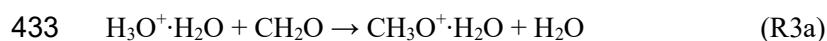
434 At room temperature, the rate coefficient of this reaction has been estimated to be $(2.65\pm0.35)\times10^{-9}$ cm^3 s^{-1}
435 calculated from the average of literature values, (Bohme et al., 1979; Midey et al., 2000), and the error
436 corresponds to the standard deviation of the measurements. The rate coefficient of the back reaction (R3b)
437 was estimated to be around six times lower $(4.4\pm1.1)\times10^{-10}$ cm^3 s^{-1}

438 $$CH_3O^+·H_2O + H_2O \rightarrow H_3O^+·H_2O + CH_2O \qquad (R3b)$$
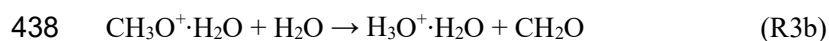
439 Reaction 3 is expected to be highly sensitive on RH, i.e. the water concentrations in the flow tube. On one
440 side, the increase in water concentration will increase the concentration of $H_3O^+·H_2O$ enhancing (R3a), on
441 the other side the excess of water compared to FM enhances (R3b). Therefore, the impact of (R3) in the ion
442 chemistry occurring in the flow tube of SIFT-MS is linked with the relative ratio of I_{37}/I_{19}. However, as
443 abovementioned, under SC the calibration factor at m/z 31 remains constant within the experimental
444 uncertainties and the RH range studied (0 -70 %), and thus (R3) seems to have insignificant impact on the
445 sensitivity of the instrument. However, in case of CC where the I_{37}/I_{19} is greater than 0.55, the gradual
446 reduction in FM sensitivity could be due to the competition between (R2a) and (R3a).
447 An alternative pathway of PMH formation is through (R4) in presence of a third body and water molecules:

448 $$CH_3O^+ + H_2O + M \rightarrow CH_3O^+·H_2O + M \qquad (R4)$$
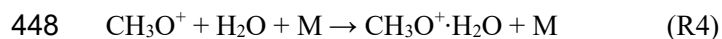
449 Reaction 4 is an association reaction competitive with (R2b) and depends on the total pressure of the
450 reaction system and the kinetic energy of reactants. In the presence of a third body, the FM-H$^+$ and water
451 molecules can lose part of their energy through collisions and further stabilize to form PMH increasing the
452 rate coefficient k_4. Therefore, it is expected that the rate coefficient of this association reaction is enhanced
453 with increasing pressure. Under a given pressure, k_4 is reduced as KE_{cm} increases because the third body
454 fails to stabilize reactants. Hansel et al. (1997) have studied the pressure dependence of the rate coefficient
455 k_4 at 0.05 eV; i.e. with KE_{cm} values similar with SIFT-MS SC used in the present study. The rate coefficient

456 of the ternary association at room temperature proposed by these authors was $k_4 = 5.7 \times 10^{-28}$ cm^6 s^{-1}. They
457 concluded that for KE_{cm} greater than 0.06 eV k_4 is negligible compared to k_{2b}. For that reason, this reaction
458 is not taken into account in most of PTR-MS studies. Nevertheless, (R4) could contribute to SIFT-MS
459 response.
460 Indeed, we estimated that under SC and CC of SIFT-MS, the binary rate coefficient of the association
461 reaction at room temperature and the established pressures is greater than 1.2 10^{-11} cm^3 s^{-1} and thus higher
462 than k_{2b} (Table 3). This value is calculated as the product of k_4 with the number density inside the flow tube
463 of SIFT-MS. However, it remains around 260 times lower than FM protonation. At this point it should be
464 noted that the value of 1.2 10^{-11} cm^{3}s^{-1} should be considered as un upper limit of the contribution of k_4
465 reaction, since under both SC and CC the flow tube was operated above room temperature, and thus lower
466 rate coefficient for k_4 is anticipated (ternary association reactions decrease with increasing temperature).
467 The importance of (R4) is expected to be enhanced at high water concentrations. Hansel et al. (1997),
468 reported that k_4 is increasing from dry to low concentrations of water reaching a maximum value, and then
469 decreases with the extra addition of water due to (R3b), which is around 37 times faster than (R4). Note
470 that absolute values cannot be extrapolated from their data. To determine the role of (R4) it is essential to
471 remind that it is competitive with (R1) for hydronium ion formation. Although k_1 has not been determined
472 for the temperatures of 323 and 393 K, considering that H$_3$O$^+$ is in high excess compared to FM, (R1) is
473 expected to be the dominant.
474 **Wrap up on Formaldehyde Determination**
475 In the case of SIFT-MS, the ion chemistry of FM is mainly controlled by (R2a) and (R2b). The increased
476 sensitivity observed under CC conditions is mainly linked to the higher k_{2a}/k_{2b} values achieved compared
477 with SC. The low kinetic energy of reactants in SIFT-MS flow tube is the reason why the sensitivity of the
478 instrument is not significantly impacted by RH. This behavior contrasts with PTR-MS. (R3) and (R4),
479 involving PMH production and inducing a lower sensitivity at the mass peak 31, seem to be of minor
480 importance or at least to be in equilibrium state for I_{37}/I_{19} below 0.55. Above that threshold, their occurrence
481 could explain a lower sensitivity but this point needs further investigations to be experimentally validated.
482 The detection limit of FM is 450 ± 50 ppt under SC. The CC allow decreasing the detection limits of the
483 SIFT MS instrument by a factor of ca. 4 for 0-50% RH (100 ppt) and by a factor of 2 under 70 % RH (200
484 ppt) (Table 2). These detection limits, based on a signal to noise ratio S/N = 3.3, are comparable or lower
485 than those reported in the PTR-MS studies that mentioned DL between 200-500 ppt with S/N = 2, (Inomata
486 et al., 2008), and DL 100 ppt under dry and 300 ppt under humid using S/N = 1, (Warneke et al., 2011),
487 and close to the most performant spectroscopic techniques noting DL around 80 ppt (Catoire et al., 2012;
488 Winkowski and Stacewicz, 2020).

489 ## 3.3 Glyoxal Determination with SIFT-MS
490
491 This section is dedicated to the evaluation of the performances of the SIFT-MS instrument to determine GL
492 in the ppb range as a function of RH. To that end, SIFT-MS is operated under both SC and CC, with a focus
493 on the chemistry of H$_3$O$^+$ and NO$^+$ ions. Note that, O$_2^+$ ion is not considered in the present study, due to
494 significant fragmentation of molecular GL induced by this ions and a subsequent lower sensitivity, strongly
495 impacted by RH.

3.3.1. Experimental Calibration of Glyoxal as a Function of RH

Figure 4 displays a typical calibration experiment of GL deploying SIFT-MS under SC and recording the mass peak 59 ($C_2H_3O_2^+$) with H_3O^+ as precursor ion. A linear response ($R^2 > 0.999$) of the instrument is noticed on the entire concentration range explored. The data points presented in Fig. 4 are obtained from two different GL syntheses and on three different days dispatched on three months. Table 4 summarizes the calibration factors and corresponding uncertainties retrieved for the mass peaks used to record GL under SC and CC.
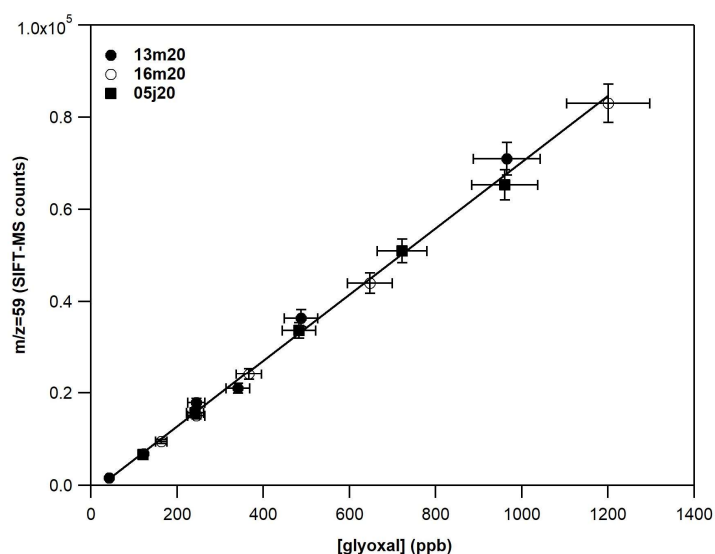
Figure 4. Calibration curves of GL at the m/z 59 derived from H_3O^+ precursor ion under dry conditions. The error bars on Y axis are 5% (extreme value) and correspond to the 2σ standard deviation of the averaged value of the SIFT-MS signal for each measurement. The errors in X axis are 8% and corresponds to the uncertainty given for the cross section value of GL (4%) and other systematic uncertainties (in the flow of the mixture, sampling flow of the instrument, etc.) added in quadrature. Circles corresponds to experiments carried out on different days (13 March 2020 and 16 March 2020) from the same gas mixture. Squares correspond to experiments carried out almost three months later (5 June 2020) with a new gas mixture and synthesis of GL.

Table 4. Calibration factors and relative ratios determined for GL under SC and CC at the m/z 59 ($C_2H_3O_2^+$) and m/z 88 ($C_2H_2O_2\cdot NO^+$) using the H_3O^+ and NO^+ precursor ions respectively. The errors quoted correspond to the 2σ precision of the fit to obtain the calibration factors.

	Standard Conditions (SC)				Custom Conditions (CC)		
I_{37}/I_{19}	Calibration factors (counts ppb^{-1})		Relative ratios	I_{37}/I_{19}	Calibration factors (counts ppb^{-1})		Relative ratios
	m/z 59 (H_3O^+)	m/z 88 (NO^+)	I_{59}/I_{88}		m/z 59 (H_3O^+)	m/z 88 (NO^+)	I_{59}/I_{88}

0.001	71.9±2.4	0.41±0.02	175	0.005	161±1	3.20±0.06	50.3
0.06	36.2±3.6	0.45±0.03	81.0	-	n.d[b]	n.d	n.d
0.09	32.0±0.9	0.44±0.03	72.7	0.28	32.9±0.5	3.41±0.07	9.6
0.27	12.1±0.6	0.48±0.05	25.2	0.56	11.4±0.1	3.68±0.18	3.1
0.41	7.6±0.7	0.50±0.03	15.2	0.79	6.9±0.1	4.30±0.05	1.6
0.54	5.5±1.0	0.52±0.02	10.5	1	4.2±0.2	4.47±0.07	0.94

515 Considering the H_3O^+ precursor ion and the mass peak 59, an increase of the sensitivity of the instrument
516 by a factor of 2 is noticed under CC compared to SC (left panel of Fig. 5). Note that a similar enhancement
517 is observed for FM (Figure 3 and Table 2). Nevertheless, the sensitivity is diminished with increasing RH
518 under both SC and CC. To evaluate whether the impact of water to GL detection is similar under both
519 operational conditions, we plotted the normalized sensitivity (calibration factor dry / calibration factor
520 humid) versus I_{37}/I_{19} ratios. , and results are also displayed in Fig. 5 (right panel). It seems that the impact
521 of water to the sensitivity of the instrument at the mass peak 59 is similar for both SC and CC. The
522 calibration factors were fitted versus the I_{37}/I_{19} ratios and the sensitivity of the instrument under SC and CC
523 are given by the following expression:

524 $$C_F^{59}(counts\ ppb^{-1}) = \frac{a}{b+\left(\frac{I_{37}}{I_{19}}\right)^c} \quad \text{Eq. (5)}$$

525 where a=2.99, b=0.04, c=1.20 for SC and a=4.53, b=0.03, c=1.74 for CC, respectively.

526 Under dry, the detection limits for GL at the mass peak 59 are determined as 280 ± 30 ppt and 120 ± 12 ppt
527 for SC and CC respectively for 1-minute integration time (Table S1 and S2). Nevertheless, with the increase
528 of relative humidity to 70% detection limits are increased up to 6 ± 1 ppb.

529

530
531
532
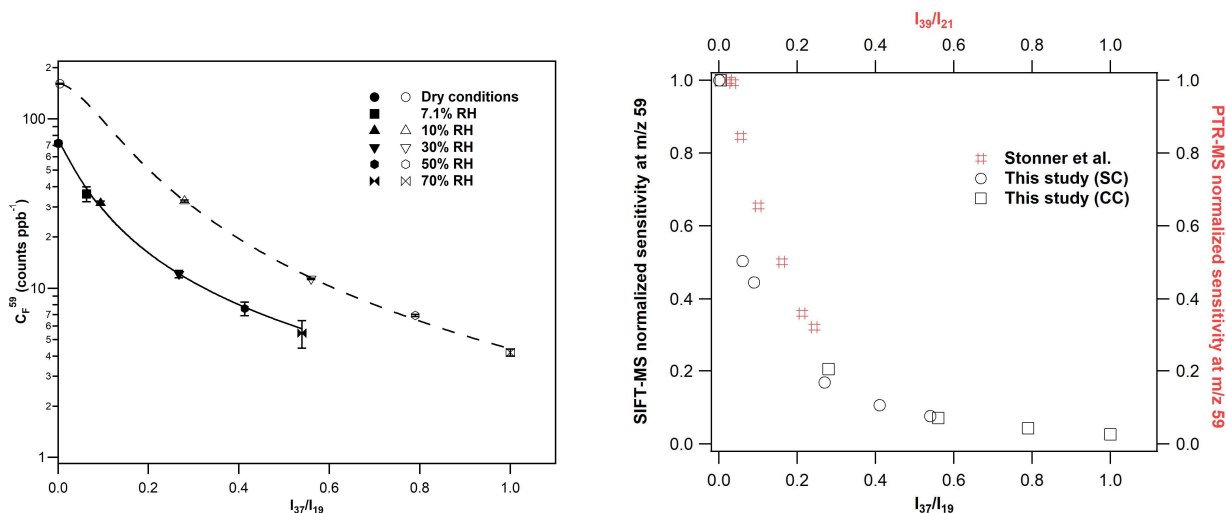
Figure 5. Left panel: calibration factors of GL at m/z 59 derived from H_3O^+ precursor ion under SC (filled symbols) and CC (open symbols) conditions. The errors quoted correspond to the 2 σ precision of the fit to obtain the calibration factors. The lines are the fitting of calibration factors with the empirical expression:

$C_F^{59}(counts\ ppb^{-1}) = \dfrac{a}{b+\left(\frac{I_{37}}{I_{19}}\right)^c}$ where for SC a=2.99, b=0.04, c=1.20 and CC a=4.53, b=0.03, c=1.74.

Right panel: GL normalized sensitivity at the mass peak 59 of SIFT-MS (in black) and PTR-MS (in red) versus the I_{37}/I_{19} and I_{39}/I_{21} ratios. For SIFT-MS, the reduction to instrument sensitivity is similar for both SC and CC conditions. For comparison purposes, the data presented in Fig. 5 of Stönner et al. (2017) study were extracted and displayed in the graph. A steeper decrease to GL sensitivity is noticed with SIFT-MS at low levels of humidity than PTR-MS.

The detection of GL was also achieved using the NO^+ precursor ion at the mass peak 88. Table 4 displays the calibration factors determined. Under SC we noticed a weaker response of the instrument using the NO^+ precursor ion compared to H_3O^+ ion. Remarkably, the introduction of water had no significant impact on the sensitivity of the mass peak 88. In fact, at the highest RH corresponding to $I_{37}/I_{19} = 0.54$, the instrument was 20% more sensitive than under dry. Operating the instrument under CC, increased by a factor of eight the sensitivity at the mass peak 88. Again, the introduction of water improved the detection of GL at the mass peak 88, by around 28% this time. Interestingly, as displayed in Table 4 at high water concentrations, peak 88 is more sensitive than mass peak 59.

3.3.2. Comparison of Glyoxal Determination between SIFT-MS and PTR-MS

There are only a few studies in literature exploring the measurement of GL using PTR-MS. Thalman et al. (2015) performed a thorough inter-comparison study of spectrometric and spectroscopic techniques for the detection of GL in an atmospheric simulation chamber. In their experiments authors used concentrations of GL up to 32 ppb, but they were unable to detect GL with their PTR-MS, attesting of the low sensitivity of the instrument (Thalman et al., 2015). However, in the recent study of Stönner et al. (2017), GL was detected at low concentrations deploying an Ionicon PTR-TOF-MS-8000 instrument. Interestingly these authors observed a decreasing sensitivity of the PTR-MS instrument with increasing water concentration, similarly to our study. As can be seen in Fig. 5 the decrease in GL sensitivity at the mass peak 59 is stepper in our SIFT-MS compared with PTR-MS (data are also presented in Table S3). Stönner et al. (2017), estimated the detection limits for GL at 250 ppt under dry and 700 ppt at the highest level of RH used.

Ion Chemistry Involved in Glyoxal Measurement with H_3O^+ Precursor Ion

Considering the ion chemistry of H_3O^+, the protonation of GL can occur through the following reaction:

$$H_3O^+ + C_2H_2O_2 \rightarrow C_2H_3O_2^+ + H_2O \qquad\qquad (R5a)$$
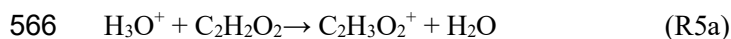
The rate coefficient of (R5a), k_{5a} is 1.9×10^{-9} cm^3 s^{-1} and is competitive with hydronium formation (reaction 1). Due to the low proton affinity of GL the deprotonization reaction is expected to occur as reported by (R5b):

$$C_2H_3O_2^+ + H_2O \rightarrow H_3O^+ + C_2H_2O_2 \qquad\qquad (R5b)$$
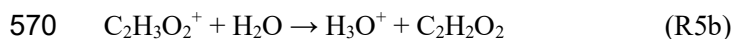
The rate coefficient of (R5b) has not been determined in literature, it could depend on KE_{cm}, similarly to (R2b). Considering this scenario, the increased sensitivity of the instrument under CC could be due to higher

573 k_{5a}/k_{5b} relative ratios, similarly to what is noticed for FM. The decreasing sensitivity of the SIFT-MS with

574 increasing water concentration could be also due to the competition between (R5a) and (R5b). In this case,

575 (R5b) should be relatively fast even under dry conditions. Its impact would be enhanced with the addition

576 of water to the reaction system, leading to initial reactants. Note that Stönner at al. (2017) made a similar

577 hypothesis to explain the decreased sensitivity with water concentration of their PTR-MS.

578 Another plausible explanation for the decreasing sensitivity of the SIFT-MS at the mass peak 59 with

579 increasing RH could be reaction (R6) which act competitively with (R5a), due to the increase of water

580 clustering in the flow tube of the SIFT-MS. Reaction (R6) leads to the formation of the mass peak with m/z

581 =77.

582 $H_3O^+{\cdot}H_2O + C_2H_2O_2 \rightarrow C_2H_3O_2^+{\cdot}H_2O + H_2O$     (R6)

583 To evaluate the effect of water clustering the complete mass spectrum pattern of GL (concentration of 300

584 ppb) was recorded for all RH levels under SC and CC. Typical normalized spectra under CC for dry and

585 50% of RH are presented in Fig. S4. Note that CC operational conditions enhance the water clustering due

586 to the lower temperature and higher pressure in the flow tube (reflected also in the I_{37}/I_{19} ratios). Under dry

587 conditions, the main peak observed is the m/z =59. The intensity of the m/z =77 corresponds solely to 1%

588 of the peak 59. Interestingly a peak at m/z =31 was observed corresponding to ca. 14% of the peak 59.

589 Under 50% of RH the intensity of the mass peak 59 is diminished and the primary peak in the mass spectrum

590 is the 31. However, the mass peak 77 is not impacted by RH and has a similar absolute intensity with dry.

591 Therefore, our results clearly demonstrated that the decrease of the instrument sensitivity in the mass 59

592 with increasing RH is not due to water clustering and thus reaction (R6) has a negligible contribution in the

593 sensitivity of our SIFT-MS.

594 The observation of the mass peak 31 in the mass spectrum of GL could arise from the fragmentation of

595 protonated GL ($C_2H_3O_2^+$ or GL-H$^+$) to protonated FM (CH_3O^+ or FM-H$^+$, with m/z =31) inside the flow

596 tube. The latter has been observed in the drift tube of the PTR-MS used by Stönner et al (2017). Authors

597 report a considerably larger signal on FM-H$^+$ than GL-H$^+$. In a recent study, Lacko et al. (2020) studied the

598 fragmentation of GL-H$^+$ deploying a SIFT-MS. The authors evidenced the strong impact of water

599 concentration on GL-H$^+$ fragmentation leading to FM-H$^+$. Interestingly, they have not observed FM-H$^+$

600 under dry conditions. Thus, authors proposed that it should be formed only in the presence of water. Similar

601 conclusions are reported by Michel et al. (2005). Finally, Lacko et al. (2020) combined their experimental

602 observations with numerical modeling and proposed a sequence of reactions to explain the fragmentation

603 of GL-H$^+$ to FM-H$^+$. The discussion of these reaction pathways is beyond the scope of this study,

604 nevertheless to feed the discussion of the manuscript we present them with the following simple expression

605 reported by (R7):

606 $C_2H_3O_2^+ + H_2O + M \rightarrow CH_3O^+ + \text{products}$   (R7)
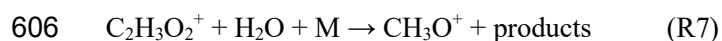
607 In this study we have further explored the possible fragmentation of GL-H$^+$ to FM-H$^+$. These experiments

608 have been performed under both SC and CC. Note that our observations were found to be independent of

609 GL concentration introduced. First we discuss our observations under SC and then under CC. The left panel

610 of Fig. 6 displays the variation of the signals recorded for FM-H$^+$ and GL-H$^+$ with I_{37}/I_{19} ratios. For

611 comparison purposes we present the normalized signals versus H factor as determined in the study of Lacko

612 et al. (2020), i.e. Eq. (3), in the right panel of Fig. 6 (data are also given in Table S4).

613 ***Fragmentation of GL-H$^+$ under SC and dry.*** In contrast with the work of Lacko et al, we observe the
614 formation of FM-H$^+$ even under dry conditions, (Lacko et al., 2020).
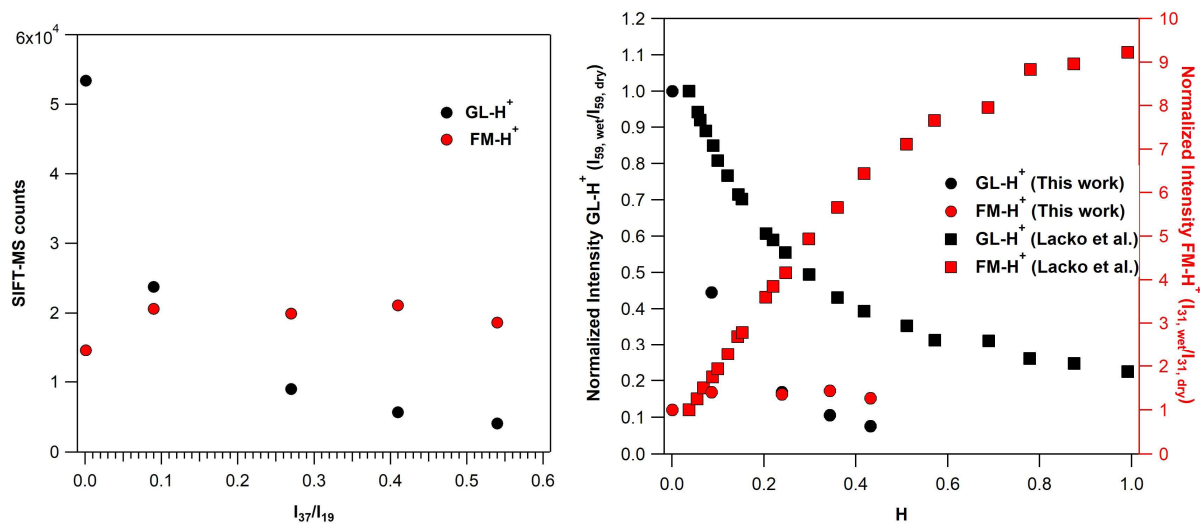
616 **Figure 6.** Left panel: SIFT-MS counts at the mass peak 59 (in black) of GL-H$^+$ and mass peak 31 (in red)
617 of FM-H$^+$ recorded by the SIFT-MS under SC conditions using around 750 ppb of GL operating the
618 instrument under SC. Right panel: Normalized sensitivity at the mass peak 59 (in black) of GL-H$^+$ and
619 mass peak 31 (in red) of FM-H$^+$, recorded with SIFT-MS under SC based on the results of the current study
620 (circles) and Lacko et al. (2020) (squares, data extracted from their Fig. 3) versus the H value Eq. (3).

621 The FM-H$^+$ signal recorded corresponds to 27 % of GL-H$^+$. Therefore, it is possible that in our SIFT-MS,
622 FM-H$^+$ is formed through alternative pathways. We propose that under our experimental conditions, GL-
623 H$^+$ can either thermally decompose inside the flow tube (operated at 393 K under SC, Table 1) or
624 fragmentizes through collisions with ions inside the flow tube leading to FM-H$^+$ (R8). Both pathways are
625 expected to be enhanced at higher temperatures and higher KE_{cm}. Note that GL-H$^+$ thermal fragmentation
626 is expected to be significantly lower in the system of Lacko et al. (2020) where the flow tube temperature
627 was 300 K, as well as in the PTR-MS where the drift tube temperature was set to 333 K and higher pressure
628 (Stönner et al., 2017).

629 $C_2H_3O_2{}^+ \rightarrow CH_3O^+ + CO$ (R8)

630 We expect that both the thermal decomposition and collision fragmentation pathways are independent of
631 the water concentration inside the SIFT flow tube. At this point it should be noted that possible thermal
632 decomposition of molecular GL in the sample plate or inside the flow tube should be considered negligible.
633 In particular, the most probable thermal decomposition pathway of molecular GL is through the following
634 reaction (Saito et al., 1984):

635 $C_2H_2O_2 \rightarrow CH_2O + CO$ (R9)
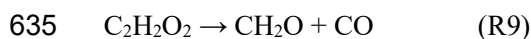
636 The molecular FM could then react with H$_3$O$^+$ through (R2a) and lead to the formation of FM-H$^+$. However,
637 the energy barrier for the thermal decomposition of the lowest transition state to give products in (R9) is
638 around 230 kJ mol^{-1}(Koch et al., 2001). Therefore, it is unlikely to occur at these temperatures and in our

system. To further validate this point, we have performed a series of experiments introducing GL inside the optical cell of the FTIR spectrometer operated at 393 K and recording sequential spectra of GL for several hours. No thermal decomposition was noticed as previously reported in literature (Feierabend et al., 2008).

Fragmentation of GL-H$^+$ under SC and humid. Increasing the water concentration from dry to 10 % of RH (corresponding to an increase by a factor of 90 to the I_{37}/I_{19} ratios, Table 4) the signal of GL-H$^+$ is reduced by 56 %, while the formation of FM-H$^+$ is enhanced by 40% (see also Fig. 6). This clearly shows that water plays a role in the formation of FM-H$^+$ to the reduced sensitivity of GL and processes proposed by Lacko et al. (2020), (R7) are probably taking place. Further increase of water concentrations in the flow tube had no impact on the formation FM-H$^+$ but GL sensitivity is still reduced. Essentially, using SIFT-MS under SC conditions, the formation of FM-H$^+$ is less impacted by water concentrations than other literature studies. Indeed, as displayed in the right panel of Fig. 6 although the GL sensitivity loss is steeper in our study compared to Lacko et al. (2020), the corresponding formation of FM-H$^+$ is substantially lower.
To conclude under SC conditions, the fragmentation of GL-H$^+$ to FM-H$^+$ occurs in the flow tube of the SIFT-MS, but it is less impacted by water concentrations than PTR-MS. Alternatively, we propose that GL-H$^+$ decomposes either thermally or through ion collisions leading to FM-H$^+$. Therefore, it seems that the abrupt loss of GL sensitivity with water concentrations is mainly due to the competition of (R5a) and (R5b). Especially under the temperature of 393 K, the deprotonization (R5b) is expected to be faster than room temperature and to play a more significant role than in the work of Lacko et al. (2020).

Fragmentation of GL-H$^+$ under CC and dry. Under custom conditions (CC) of the SIFT-MS, the formation of FM-H$^+$ from the fragmentation of GL-H$^+$, is also observed. Nevertheless, the ratio of FM-H$^+$ to GL-H$^+$ signals is significantly diminished. Indeed, under dry conditions the fragmentation is reduced from 27 % to ca. 14 % for SC and CC respectively. This observation supports our previous hypothesis: GL-H$^+$ could decompose inside our SIFT-MS flow tube. Both the temperature decrease and pressure increase, changing from SC to CC, tend to suppress the decomposition of GL-H$^+$.

Fragmentation of GL-H$^+$ under CC and humid. A similar reduction of the fragmentation of GL-H$^+$ was noticed in presence of water when comparing the signals recorded under SC and CC for I_{37}/I_{19} equal to 0.27±0.01 and 0.55±0.01. As displayed in Fig. S3 the decreased sensitivity of GL is similar under both SC and CC. Note that Fig. S3 should be viewed as a way to compare the impact of water concentrations on the fragmentation of GL-H$^+$ and the appearance of FM-H$^+$. Essentially, the impact of water to the sensitivity of SIFT-MS to GL is independent on the operational conditions of the instrument. However, with the increase of water concentration inside the flow tube from dry to a value of 0.28 for I_{37}/I_{19} ratio (an increase by a factor of 56) the signal of FM-H$^+$ increases by almost a factor of 3. Therefore, water plays a more important role to the presence of FM-H$^+$ under CC and we anticipate that reactions proposed by Lacko et al. (2020) can dominate (R7). Further increase of water concentration in the flow tube reduced the signal of FM-H$^+$. Although this looks as a paradox and in contradiction with the abovementioned discussion, we suggest that this decrease is related to the competition between the (R7) and (R8), i.e. the deprotonization reaction of FM-H$^+$ (R2b). Nevertheless, a more thorough investigation is necessary to support this point.
Therefore, we propose that the increased sensitivity of the instrument under CC is mainly due to higher k_{5a}/k_{5b} ratios. The expected lower values of this k_{5a}/k_{5b} ratio could explain the lower sensitivity to detect GL in the presence of water. Nevertheless, the decreasing GL sensitivity with increasing RH could be also

682   attributed to fragmentation of GL-H$^+$ to FM-H$^+$, both linked to thermal decomposition and reactions
683   involving water molecules as discussed by Lacko et al. (2020).

684   **Ion Chemistry Involved in Glyoxal Measurement using NO$^+$ Precursor Ion**
685   The detection of GL in the flow tube of the SIFT-MS proceeds through the following reaction:

686    $NO^+ + C_2H_2O_2 + M \rightarrow C_2H_2O_2 \cdot NO^+$ (R10)
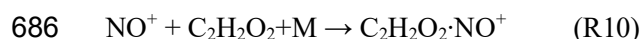
687   The rate coefficient measured at room temperature for (R10) is 8 x10^{-11} cm^3 s^{-1},(Michel et al., 2005) i.e.
688   around 24 times below the protonation reaction of GL (R5a). The latter could explain the reduced sensitivity
689   at the mass peak 88 compared to the mass 59 under dry conditions. Furthermore, (R10) is a three-body
690   association reaction. In an association process, an intermediate species is formed before the formation of
691   final products. The stability of this intermediate is both temperature and pressure dependent, and determines
692   the overall rate coefficient of the reaction. The increased sensitivity to the detection of GL under custom
693   conditions, is related with the temperature and pressure conditions existing in the flow tube. In particular
694   the decrease of the flow tube temperature combined with a 20% increase in the total pressure (from 0.65 to
695   0.85 Torr) resulted in a better stabilization of the adduct that leads to product formation for (R10), and thus
696   improved sensitivity. Apparently under our experimental conditions the reaction of NO$^+$ with GL is in the
697   exponential part of a typical fall-off graph of an association reaction (Guimbaud et al., 2007).
698   The positive impact of water concentrations on the detection of GL at the mass peak 88, could be linked
699   with the formation of H$_2$O·NO$^+$ hydrate cluster at the mass peak 48. Indeed, we have observed an increase
700   to the abundance of the cluster with increasing RH. The following reaction could be proposed:

701    $H_2O \cdot NO^+ + C_2H_2O_2 + M \rightarrow C_2H_2O_2 \cdot NO^+ + H_2O$ (R11)
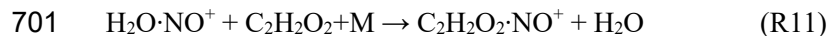
702   Although the rate coefficient of (R10) has not been measured in literature, it has been showed that the
703   reactions of H$_2$O·NO$^+$ with several VOCs are just as fast as or even faster than those with NO$^+$ ion (Michel
704   et al., 2005). Mass scan spectra using the NO$^+$ ion were also collected but besides the mass peak 88, no
705   other peaks that could be attributed to GL were observed.

706 # 4. Conclusions

707   SIFT-MS appears to be a powerful and reliable analytical tool for the real-time quantification of FM in
708   laboratory studies and outdoor/indoor field environments. Remarkably, under SC the sensitivity of the
709   instrument is not impacted by RH with a corresponding detection limit of ca. 500 ppt. Operating the
710   instrument under CC increased the sensitivity however, for I_{37}/I_{19} above 0.58 the sensitivity is reduced and
711   a correction factor should be applied. We recommend the operation of SIFT-MS under SC for the
712   measurement of ambient FM greater than 500 ppt. Furthermore, our strategy to operate the SIFT-MS
713   instrument under different modes, allowed us to shed light on the ion chemistry occurring in the flow tube
714   and to identify the key reactions and processes that define the sensitivity of the instrument towards FM. A
715   thorough comparison of our observations with literature studies carried out with PTR-MS, evidences that
716   the strong decay of PTR-MS sensitivity with increasing RH is related to the application of the electrical
717   field in the DRIFT tube. It enhances the rate coefficient of deprotonization reaction of FM. Regarding GL,
718   we have performed a detailed research on the ion chemistry related with H$_3$O$^+$ and NO$^+$ ions. Regarding

719 H_3O^+ we evidenced a sharp decrease of the instrument sensitivity with increasing RH, similar to previous
720 PTR-MS and SIFT-MS studies, due to GL-H$^+$ fragmentation. Nevertheless, based on our experimental
721 observations we propose alternative pathways of GL-H$^+$ fragmentation, such as GL-H$^+$ decomposition,
722 which seems to be of greater importance than it has been considered previously in literature. Based on the
723 detection limits achieved with the H_3O^+ ion, we suggest that SIFT-MS is not able to monitor GL in outdoor
724 ambient air due to the strong impact of RH on SIFT-MS sensitivity. It should be clarified that as shown in
725 Figure 5, the fitting of calibration factors with I_{37}/I_{19} ratio is feasible (see figure 5 caption) and thus the
726 concentrations of glyoxal can be retrieved even under environments where the RH changes during the
727 experiment by following the I_{37}/I_{19} ratio. Therefore, the major limitation is the instrument sensitivity and
728 not the variation of the RH of the ambient environment. On the contrary, SIFT-MS can be deployed
729 efficiently in laboratory scale studies (i.e. atmospheric simulation chambers, photochemical reactors) or
730 indoor experimental rooms where GL concentrations are in the ppb range. In addition, we recommend that
731 using the H_3O^+ ion for the monitoring of GL concentrations should be performed with great caution due to
732 the strong RH dependence and contribution on the signal of FM-H$^+$. Nevertheless, deploying NO$^+$ precursor
733 ion for the monitoring of GL seems to be ideal since the sensitivity of the instrument is slightly impacted
734 by RH. The GL detection limits using NO$^+$ are in the ppb range, however, we evidence that slight pressure
735 increase in the flow tube of the instrument can result to a vigorous increase to instrument sensitivity.
736 Certainly, our research on the NO$^+$ chemistry opens new pathways for GL quantification and detection in
737 ambient air deploying soft ionization techniques, such as PTR-MS with NO$^+$ ion, which are generally
738 operated at higher pressures than SIFT-MS. Ultimately, our observations indicate that there is potential for
739 sensitivity improvement for the SIFT-MS, and that it should be considered as a promising tool for the real-
740 time monitoring of VOCs with low proton transfer affinity.

5. List of abbreviations

742 CC: Custom operational conditions of the SIFT-MS
743 C_F^{31}: calibration factor of formaldehyde at the mass peak 31
744 C_F^{59}: calibration factor of glyoxal at the mass peak 59
745 D: Internal diameter of the flow tube
746 DL: Detection limit
747 DNPH: Dinitrophenylhydrazine
748 DOAS: Differential optical absorption spectroscopy
749 EAR: Electron attachment reaction
750 ε: Distance for a full mixing of neutral molecules with the carrier gas in the flow tube
751 F_g: Carrier gas flow rate,
752 F_{H_2O}: Sample flow of pure water in the sample flow
753 F_{total}: Total flow rate inside the flow tube
754 F_{VOC}: Sample flow of pure VOC (formaldehyde or glyoxal) in the sample flow
755 FM: Formaldehyde
756 FM-H$^+$: Protonated formaldehyde
757 FTIR spectroscopy: Fourier transform infrared spectroscopy
758 GL: Glyoxal
759 GL-H$^+$: Protonated glyoxal
760 HPLC: High-performance liquid chromatography

761 IBBCEAS: incoherent broadband cavity-enhanced absorption spectrometer
762 k_B: Boltzmann constant
763 KE_{cm}: Mean kinetic energy between reactants
764 KE_{ion}: Kinetic energy of ions
765 L: Length of the flow tube
766 m and M:Masses of the carrier gas and the neutral reactant, respectively
767 M_{ion}: Mass of reactant ion
768 MFC: Mass flow controler
769 N: Molecular density in the flow tube
770 SC: Standard operational conditions of the SIFT-MS
771 SIFT-MS: Selected ion flow tube mass spectrometer
772 SOA: Secondary aerosol formation
773 P_g: Pressure in flow tube
774 PMH: Protonated methyl hydroperoxide
775 PTR-MS: Proton transfer mass spectrometry
776 RH: Relative humidity
777 TDLAS: Tunable-diode laser absorption spectrometer
778 t_r: Reaction time inside the flow tube of the SIFT-MS
779 T_g: Flow tube temperature
780 v_g: Carrier gas velocity
781 v_i: Ions flow velocity
782 $[H_2O]$: H$_2$O concentration in the flow tube
783 $[VOC]$: VOC (i.e. formaldehyde or glyoxal) concentration in the flow tube
784
785

Data availability

787 All relevant data and supporting information have been provided in the Supplement.
788

Author contribution

790 AZ realization of experiments, data treatment. MNR designing of experiments, data treatment and
791 manuscript writing. FT designing of experiments and manuscript writing.
792

Competing interests

794 The authors declare that they have no conflict of interest.
795

Acknowledgements

797 This work was achieved in the frame of CLIMDO project funded by ANR under contract (ANR-19-CE01-
798 0008), Labex CaPPA, funded by ANR through the PIA under contract ANR-11-LABX-0005-01, and CPER
799 CLIMIBIO project, both funded by the Hauts-de-France Regional Council and the European Regional
800 Development Fund (ERDF).

801

References

Allani, A., Bedjanian, Y., Papanastasiou, D. K., and Romanias, M. N.: Reaction Rate Coefficient of OH Radicals with d9-Butanol as a Function of Temperature, ACS Omega, 6, 18123-18134, https://doi.org/10.1021/acsomega.1c01942, 2021.

Atkinson, R.: Atmospheric Chemistry of VOCs and NOx, Atmos. Environ., 34, 2063-2101, https://doi.org/10.1016/S1352-2310(99)00460-4, 2000.

Ban-Weiss, G. A., McLaughlin, J. P., Harley, R. A., Kean, A. J., Grosjean, E., and Grosjean, D.: Carbonyl and Nitrogen Dioxide Emissions From Gasoline- and Diesel-Powered Motor Vehicles, Environ. Sci. Technol., 42, 3944-3950, https://doi.org/10.1021/es8002487, 2008.

Bernstein, R. S., Stayner, L. T., Elliott, L. J., Kimbrough, R., Falk, H., and Blade, L. E. O.: Inhalation Exposure to Formaldehyde: An Overview of Its Toxicology, Epidemiology, Monitoring, and Control, Am. Ind. Hyg, 45, 778-785, https://doi.org/10.1080/15298668491400601, 1984.

Bierbaum, V. M., Golde, M. F., and Kaufman, F.: Flowing Afterglow Studies of Hydronium Ion Clustering Including Diffusion Effects, J. Chem. Phys., 65, 2715-2724, https://doi.org/10.1063/1.433415, 1976.

Bohme, D. K., Mackay, G. I., and Tanner, S. D.: An Experimental Study of the Gas-Phase Kinetics of Reactions with Hydrated Hydronium(1+) Ions(n = 1-3) at 298 K, J. Am. Chem. Soc., 101, 3724-3730, https://doi.org/10.1021/ja00508a003, 1979.

Bolden, R. C. and Twiddy, N. D.: A Flowing Afterglow Study of Water Vapour, Faraday Discuss. Chem. Soc., 53, 192-200, https://doi.org/10.1039/DC9725300192, 1972.

Caron, A., Redon, N., Thevenet, F., Hanoune, B., and Coddeville, P.: Performances and limitations of electronic gas sensors to investigate an indoor air quality event, Build. Environ., 107, 19-28, https://doi.org/10.1016/j.buildenv.2016.07.006, 2016.

Caron, F., Guichard, R., Robert, L., Verriele, M., and Thevenet, F.: Behaviour of individual VOCs in indoor environments: How ventilation affects emission from materials, Atmos. Environ., 243, 117713, https://doi.org/10.1016/j.atmosenv.2020.117713, 2020.

Catoire, V., Bernard, F., Mébarki, Y., Mellouki, A., Eyglunent, G., Daële, V., and Robert, C.: A Tunable Diode Laser Absorption Spectrometer for Formaldehyde Atmospheric Measurements Validated by Simulation Chamber Instrumentation, J. Environ. Sci., 24, 22-33, https://doi.org/10.1016/S1001-0742(11)60726-2, 2012.

Coburn, S., Ortega, I., Thalman, R., Blomquist, B., Fairall, C. W., and Volkamer, R.: Measurements of Diurnal Variations and Eddy Covariance (EC) Fluxes of Glyoxal in the Tropical Marine Boundary Layer: Description of the Fast LED-CE-DOAS Instrument, Atmos. Meas. Tech., 7, 3579-3595, https://doi.org/10.5194/amt-7-3579-2014, 2014.

Crump, D. R., Squire, R. W., and Yu, C. W. F.: Sources and Concentrations of Formaldehyde and Other Volatile Organic Compounds in the Indoor Air of Four Newly Built Unoccupied Test Houses, Indoor Built Environ., 6, 45-55, https://doi.org/10.1177/1420326x9700600106, 1997.

Feierabend, K. J., Zhu, L., Talukdar, R. K., and Burkholder, J. B.: Rate Coefficients for the OH + HC(O)C(O)H (Glyoxal) Reaction between 210 and 390 K, J. Phys. Chem. A., 112, 73-82, https://doi.org/10.1021/jp0768571, 2008.

Fu, T.-M., Jacob, D. J., Wittrock, F., Burrows, J. P., Vrekoussis, M., and Henze, D. K.: Global Budgets of Atmospheric Glyoxal and Methylglyoxal, and Implications for Formation of Secondary Organic Aerosols, J. Geophys. Res. Atmos., 113, https://doi.org/10.1029/2007JD009505, 2008.

Gómez Alvarez, E., Moreno, M. V., Gligorovski, S., Wortham, H., and Cases, M. V.: Characterisation and Calibration of Active Sampling Solid Phase Microextraction Applied to Sensitive Determination of Gaseous Carbonyls, Talanta, 88, 252-258, https://doi.org/10.1016/j.talanta.2011.10.039, 2012.

851 Grosjean, D., Grosjean, E., and Gertler, A. W.: On-Road Emissions of Carbonyls from Light-
852 Duty and Heavy-Duty Vehicles, Environ. Sci. Technol, 35, 45-53,
853 https://doi.org/10.1021/es001326a, 2001.
854 Guimbaud, C., Catoire, V., Bergeat, A., Michel, E., Schoon, N., Amelynck, C., Labonnette, D.,
855 and Poulet, G.: Kinetics of the reactions of acetone and glyoxal with O2+ and NO+ ions and
856 application to the detection of oxygenated volatile organic compounds in the atmosphere by
857 chemical ionization mass spectrometry, I. J. of Mass Spectrom., 263, 276-288,
858 https://doi.org/10.1016/j.ijms.2007.03.006, 2007.
859 Hansel, A., Singer, W., Wisthaler, A., Schwarzmann, M., and Lindinger, W.: Energy
860 Dependencies of the Proton Transfer Reactions $H_3O^+ + CH_2O \Leftrightarrow CH_2OH^+ + H_2O$, Int. J. Mass
861 Spectrom. Ion Process, 167-168, 697-703, https://doi.org/10.1016/S0168-1176(97)00128-6,
862 1997.
863 Hays, M. D., Geron, C. D., Linna, K. J., Smith, N. D., and Schauer, J. J.: Speciation of Gas-
864 Phase and Fine Particle Emissions from Burning of Foliar Fuels, Environ. Sci. Technol., 36,
865 2281-2295, https://doi.org/10.1021/es0111683, 2002.
866 Inomata, S., Tanimoto, H., Kameyama, S., Tsunogai, U., Irie, H., Kanaya, Y., and Wang, Z.:
867 Technical Note: Determination of Formaldehyde Mixing Ratios in air with PTR-MS: Laboratory
868 Experiments and Field Measurements, Atmos. Chem. Phys., 8, 273-284,
869 https://doi.org/10.5194/acp-8-273-2008, 2008.
870 Kaiser, J., Wolfe, G. M., Bohn, B., Broch, S., Fuchs, H., Ganzeveld, L. N., Gomm, S., Häseler,
871 R., Hofzumahaus, A., Holland, F., Jäger, J., Li, X., Lohse, I., Lu, K., Prévôt, A. S. H., Rohrer, F.,
872 Wegener, R., Wolf, R., Mentel, T. F., Kiendler-Scharr, A., Wahner, A., and Keutsch, F. N.:
873 Evidence for an Unidentified Non-Photochemical Ground-Level Source of Formaldehyde in the
874 Po Valley with Potential Implications for Ozone Production, Atmos. Chem. Phys., 15, 1289-
875 1298, https://doi.org/10.5194/acp-15-1289-2015, 2015.
876 Kean, A. J., Grosjean, E., Grosjean, D., and Harley, R. A.: On-Road Measurement of Carbonyls
877 in California Light-Duty Vehicle Emissions, Environ. Sci. Technol, 35, 4198-4204,
878 https://doi.org/10.1021/es010814v, 2001.
879 Kefauver, S. C., Filella, I., and Peñuelas, J.: Remote Sensing of Atmospheric Biogenic Volatile
880 Organic Compounds (BVOCs) via Satellite-Based Formaldehyde Vertical Column Assessments,
881 Int. J. Remote Sens., 35, 7519-7542, https://doi.org/10.1080/01431161.2014.968690, 2014.
882 Kim, K.-H., Jahan, S. A., and Lee, J.-T.: Exposure to Formaldehyde and Its Potential Human
883 Health Hazards, J. Environ. Sci. Health C, 29, 277-299,
884 https://doi.org/10.1080/10590501.2011.629972, 2011.
885 Koch, D. M., Khieu, N. H., and Peslherbe, G. H.: Ab Initio Studies of the Glyoxal Unimolecular
886 Dissociation Pathways, J. Phys. Chem. A., 105, 3598-3604, https://doi.org/10.1021/jp0039013,
887 2001.
888 Lacko, M., Piel, F., Mauracher, A., and Španěl, P.: Chemical Ionization of Glyoxal and
889 Formaldehyde with H_3O^+ Ions using SIFT-MS Under Variable System Humidity, Phys. Chem.
890 Chem. Phys., 22, 10170-10178, https://doi.org/10.1039/D0CP00297F, 2020.
891 Langer, S., Bekö, G., Bloom, E., Widheden, A., and Ekberg, L.: Indoor air quality in passive and
892 conventional new houses in Sweden, Build. Environ., 93, 92-100,
893 https://doi.org/10.1016/j.buildenv.2015.02.004, 2015.
894 Lee, M., Heikes, B. G., Jacob, D. J., Sachse, G., and Anderson, B.: Hydrogen Peroxide,
895 Organic Hydroperoxide, and Formaldehyde as Primary Pollutants from Biomass Burning, J.
896 Geophys. Res. Atmos., 102, 1301-1309, https://doi.org/10.1029/96JD01709, 1997.
897 Li, Z., Schwier, A. N., Sareen, N., and McNeill, V. F.: Reactive Processing of Formaldehyde and
898 Acetaldehyde in Aqueous Aerosol Mimics: Surface Tension Depression and Secondary Organic
899 Products, Atmos. Chem. Phys., 11, 11617-11629, https://doi.org/10.5194/acp-11-11617-2011,
900 2011.

Liggio, J., Li, S.-M., and McLaren, R.: Reactive Uptake of Glyoxal by Particulate Matter, J. Geophys. Res. Atmos., 110, https://doi.org/10.1029/2004JD005113, 2005.

Liu, J., Li, X., Yang, Y., Wang, H., Wu, Y., Lu, X., Chen, M., Hu, J., Fan, X., Zeng, L., and Zhang, Y.: An IBBCEAS System for Atmospheric Measurements of Glyoxal and Methylglyoxal in the Presence of High NO_2 Concentrations, Atmos. Meas. Tech., 12, 4439-4453, https://doi.org/10.5194/amt-12-4439-2019, 2019.

Liu, W., Zhang, J., Zhang, L., Turpin, B. J., Weisel, C. P., Morandi, M. T., Stock, T. H., Colome, S., and Korn, L. R.: Estimating contributions of indoor and outdoor sources to indoor carbonyl concentrations in three urban areas of the United States, Atmos. Environ., 40, 2202-2214, https://doi.org/10.1016/j.atmosenv.2005.12.005, 2006.

Lu, X.-W., Jiang, L.-X., Liu, J., Yang, Y., Liu, Q.-Y., Ren, Y., Li, X., and He, S.-G.: Sensitive Detection of Gas-Phase Glyoxal by Electron Attachment Reaction Ionization Mass Spectrometry, Anal. Chem., 91, 12688-12695, https://doi.org/10.1021/acs.analchem.9b02029, 2019.

Luecken, D. J., Hutzell, W. T., Strum, M. L., and Pouliot, G. A.: Regional Sources of Atmospheric Formaldehyde and Acetaldehyde, and Implications for Atmospheric Modeling, Atmos. Environ., 47, 477-490, https://doi.org/10.1016/j.atmosenv.2011.10.005, 2012.

Mahajan, A. S., Prados-Roman, C., Hay, T. D., Lampel, J., Pöhler, D., Großmann, K., Tschritter, J., Frieß, U., Platt, U., Johnston, P., Kreher, K., Wittrock, F., Burrows, J. P., Plane, J. M. C., and Saiz-Lopez, A.: Glyoxal Observations in the Global Marine Boundary Layer, J. Geophys. Res. Atmos., 119, 6160-6169, https://doi.org/10.1002/2013JD021388, 2014.

Michel, E., Schoon, N., Amelynck, C., Guimbaud, C., Catoire, V., and Arijs, E.: A Selected Ion Flow Tube Study of the Reactions of H_3O^+, NO^+ and O_2^+ with Methyl Vinyl Ketone and Some Atmospherically Important Aldehydes, Int. J. Mass Spectrom., 244, 50-59, https://doi.org/10.1016/j.ijms.2005.04.005, 2005.

Midey, A. J., Arnold, S. T., and Viggiano, A. A.: Reactions of $H_3O^+(H_2O)n$ with Formaldehyde and Acetaldehyde, J. Phys. Chem. A., 104, 2706-2709, https://doi.org/10.1021/jp993797t, 2000.

Myriokefalitakis, S., Vrekoussis, M., Tsigaridis, K., Wittrock, F., Richter, A., Brühl, C., Volkamer, R., Burrows, J. P., and Kanakidou, M.: The influence of natural and anthropogenic secondary sources on the glyoxal global distribution, Atmos. Chem. Phys., 8, 4965-4981, https://doi.org/10.5194/acp-8-4965-2008, 2008.

Osseiran, N., Romanias, M. N., Gaudion, V., Angelaki, M. E., Papadimitriou, V. C., Tomas, A., Coddeville, P., and Thevenet, F.: Development and Validation of a Thermally Regulated Atmospheric Simulation Chamber (THALAMOS): A Versatile Tool to Simulate Atmospheric Processes, J. Environ. Sci., 95, 141-154, https://doi.org/10.1016/j.jes.2020.03.036, 2020.

Rossignol, S., Aregahegn, K. Z., Tinel, L., Fine, L., Nozière, B., and George, C.: Glyoxal Induced Atmospheric Photosensitized Chemistry Leading to Organic Aerosol Growth, Environ. Sci. Technol., 48, 3218-3227, https://doi.org/10.1021/es405581g, 2014.

Saito, K., Kakumoto, T., and Murakami, I.: Thermal Unimolecular Decomposition of Glyoxal, J. Phys. Chem., 88, 1182-1187, https://doi.org/10.1021/j150650a033, 1984.

Salter, R. J., Blitz, M. A., Heard, D. E., Kovács, T., Pilling, M. J., Rickard, A. R., and Seakins, P. W.: Quantum yields for the photolysis of glyoxal below 350 nm and parameterisations for its photolysis rate in the troposphere, Phys. Chem. Chem. Phys., 15, 4984-4994, https://doi.org/10.1039/C3CP43597K, 2013.

Salthammer, T.: Formaldehyde Sources, Formaldehyde Concentrations and Air Exchange Rates in European Housings, Build. Environ., 150, 219-232, https://doi.org/10.1016/j.buildenv.2018.12.042, 2019.

Sinreich, R., Coburn, S., Dix, B., and Volkamer, R.: Ship-Based Detection of Glyoxal Over the Remote Tropical Pacific Ocean, Atmos. Chem. Phys., 10, 11359-11371, https://doi.org/10.5194/acp-10-11359-2010, 2010.

951 Smith, D. and Adams, N. G.: The Selected Ion Flow Tube (Sift): Studies of Ion-Neutral
952 Reactions, in: Adv. At. Mol. Phys., edited by: Bates, D., and Bederson, B., Academic Press, 1-
953 49, https://doi.org/10.1016/S0065-2199(08)60229-8, 1988.
954 Smith, D. and Španěl, P.: Selected Ion Flow Tube Mass Spectrometry (SIFT-MS) for On-line
955 Trace Gas Analysis, Mass Spectrom. Rev., 24, 661-700, https://doi.org/10.1002/mas.20033,
956 2005.
957 Španěl, P. and Smith, D.: Selected Ion Flow Tube: a Technique for Quantitative Trace Gas
958 Analysis of Air and Breath, Med. Biol. Eng. Comput., 34, 409-419,
959 https://doi.org/10.1007/BF02523843, 1996.
960 Španěl, P. and Smith, D.: Quantitative Selected Ion Flow Tube Mass Spectrometry: The
961 Influence of Ionic Diffusion and Mass Discrimination, J. Am. Soc. Mass Spectrom., 12, 863-872,
962 https://doi.org/10.1021/jasms.8b01653, 2001.
963 Stönner, C., Derstroff, B., Klüpfel, T., Crowley, J. N., and Williams, J.: Glyoxal Measurement
964 with a Proton Transfer Reaction Time of Flight Mass Spectrometer (PTR-TOF-MS):
965 Characterization and Calibration, J. Mass Spectrom., 52, 30-35,
966 https://doi.org/10.1002/jms.3893, 2017.
967 Thalman, R., Baeza-Romero, M. T., Ball, S. M., Borrás, E., Daniels, M. J. S., Goodall, I. C. A.,
968 Henry, S. B., Karl, T., Keutsch, F. N., Kim, S., Mak, J., Monks, P. S., Muñoz, A., Orlando, J.,
969 Peppe, S., Rickard, A. R., Ródenas, M., Sánchez, P., Seco, R., Su, L., Tyndall, G., Vázquez,
970 M., Vera, T., Waxman, E., and Volkamer, R.: Instrument Intercomparison of Glyoxal, Methyl
971 Glyoxal and NO_2 Under Simulated Atmospheric Conditions, Atmos. Meas. Tech., 8, 1835-1862,
972 https://doi.org/10.5194/amt-8-1835-2015, 2015.
973 Thevenet, F., Verriele, M., Harb, P., Thlaijeh, S., Brun, R., Nicolas, M., and Angulo-Milhem, S.:
974 The indoor fate of terpenes: Quantification of the limonene uptake by materials, Build. Environ.,
975 188, 107433, https://doi.org/10.1016/j.buildenv.2020.107433, 2021.
976 Vlasenko, A., Macdonald, A. M., Sjostedt, S. J., and Abbatt, J. P. D.: Formaldehyde
977 Measurements by Proton Transfer Reaction – Mass Spectrometry (PTR-MS): Correction for
978 Humidity Effects, Atmos. Meas. Tech., 3, 1055-1062, https://doi.org/10.5194/amt-3-1055-2010,
979 2010.
980 Volkamer, R., Spietz, P., Burrows, J., and Platt, U.: High-Resolution Absorption Cross-Section
981 of Glyoxal in the UV–vis and IR Spectral Ranges, J. Photochem. Photobiol. A, 172, 35-46,
982 https://doi.org/10.1016/j.jphotochem.2004.11.011, 2005.
983 Volkamer, R., San Martini, F., Molina, L. T., Salcedo, D., Jimenez, J. L., and Molina, M. J.: A
984 Missing Sink for Gas-Phase Glyoxal in Mexico City: Formation of Secondary Organic Aerosol,
985 Geophys. Res. Lett, 34, https://doi.org/10.1029/2007GL030752, 2007.
986 Warneke, C., Veres, P., Holloway, J. S., Stutz, J., Tsai, C., Alvarez, S., Rappenglueck, B.,
987 Fehsenfeld, F. C., Graus, M., Gilman, J. B., and de Gouw, J. A.: Airborne Formaldehyde
988 Measurements Using PTR-MS: Calibration, Humidity Dependence, Inter-Comparison and Initial
989 Results, Atmos. Meas. Tech., 4, 2345-2358, https://doi.org/10.5194/amt-4-2345-2011, 2011.
990 Winkowski, M. and Stacewicz, T.: Optical Detection of Formaldehyde in Air in the 3.6 µm
991 Range, Biomed. Opt. Express, 11, 7019-7031, https://doi.org/10.1364/BOE.405384, 2020.
992 Wisthaler, A., Apel, E. C., Bossmeyer, J., Hansel, A., Junkermann, W., Koppmann, R., Meier,
993 R., Müller, K., Solomon, S. J., Steinbrecher, R., Tillmann, R., and Brauers, T.: Technical Note:
994 Intercomparison of Formaldehyde Measurements at the Atmosphere Simulation Chamber
995 SAPHIR, Atmos. Chem. Phys., 8, 2189-2200, https://doi.org/10.5194/acp-8-2189-2008, 2008.
996 Wróblewski, T., Ziemczonek, L., Alhasan, A. M., and Karwasz, G. P.: Ab Initio and Density
997 Functional Theory Calculations of Proton Affinities for Volatile Organic Compounds, Eur. Phys.
998 J. Spec. Top., 144, 191-195, https://doi.org/10.1140/epjst/e2007-00126-7, 2007.
999 Xiao, Y., Jacob, D. J., and Turquety, S.: Atmospheric Acetylene and its Relationship with CO as
1000 an Indicator of Air Mass Age, J. Geophys. Res. Atmos., 112,
1001 https://doi.org/10.1029/2006JD008268, 2007.

1002   Yuan, B., Koss, A. R., Warneke, C., Coggon, M., Sekimoto, K., and de Gouw, J. A.: Proton-
1003   Transfer-Reaction Mass Spectrometry: Applications in Atmospheric Sciences, Chem. Rev., 117,
1004   13187-13229, https://doi.org/10.1021/acs.chemrev.7b00325, 2017.
1005
1006